Check for updates

Advanced Functional Materials

ADVANCED FUNCTIONAL MATERIALS
www.afm-journal.de

RESEARCH ARTICLE OPEN ACCESS

MXene/PEDOT Functional Coatings on Flexible Microelectrode Arrays for Multianalyte In Vivo Neurochemical Sensing and Electrophysiology

Ilaria Gatti[1,2] | Karamullah Eisawi[3] | Umisha Siwakoti[1] | Greyson Jadwin[4] | Ashmita Sigdel[1] | Michela Chiappalone[2] | Deepak Kumbhare[4] | Michael Naguib[3] | Elisa Castagnola[1,5,4]

[1]Department of Biomedical Engineering, Louisiana Tech University, Ruston, Louisiana, USA | [2]Department of Computer Science, Bioengineering, Robotics and Systems Engineering (DIBRIS), University of Genoa, Genoa, Italy | [3]Department of Physics and Engineering Physics, Tulane University, New Orleans, Louisiana, USA | [4]Department of Neurosurgery, Louisiana State University Health Sciences Center Shreveport, Shreveport, Louisiana, USA | [5]Institute for Micromanufacturing, Louisiana Tech University, Ruston, Louisiana, USA

Correspondence: Michael Naguib (naguib@tulane.edu) | Elisa Castagnola (elisa@latech.edu)

Received: 16 January 2026 | **Revised:** 3 April 2026 | **Accepted:** 9 April 2026

Keywords: dopamine | glassy carbon | microelectrode arrays | MXene | neural signals | serotonin | square wave voltammetry

ABSTRACT

MXene-based coatings offer a promising route to multifunctional neural interfaces for in vivo neurochemical sensing. Here, we develop $Ti_3C_2T_x$ MXene/poly(3,4-ethylenedioxythiophene) (MXene/PEDOT) composite coatings for glassy carbon (GC) and platinum (Pt) flexible microelectrode arrays (MEAs), enabling multianalyte neurochemical sensing and electrophysiological recording. MXene/PEDOT forms uniform nanostructured films that increase charge storage capacity by one order of magnitude, reduce impedance by ~84% at 1 kHz, and enhance charge transfer efficiency for square-wave voltammetry (SWV). Using an optimized SWV waveform, functionalized GC-MEAs detect dopamine (DA) and serotonin (5-HT) individually and simultaneously with low limits of detection (9.6 nM for DA; 4.7 nM for 5-HT), high selectivity, and exceptional resistance to electrochemical fouling (>120 h DA; >40 h 5-HT) and biofouling. In vivo measurements resolve basal extracellular DA in the striatum (99 ± 29 nM) and 5-HT in the amygdala and prefrontal cortex (20 ± 7 nM), with their simultaneous striatal detection validated by pharmacological manipulation of neurotransmitter levels. Extending this strategy to Pt-MEAs confers neurochemical sensitivity while preserving single-unit recordings, establishing MXene/PEDOT as a versatile functional coating for multimodal, multianalyte interfaces.

1 | Introduction

Real-time, multimodal monitoring of neurochemical and electrophysiological activity in the living brain is essential for advancing our understanding of neural circuit function and enabling next generation neurotechnologies [1–3]. Electroactive monoamine neurotransmitters, including dopamine (DA) and serotonin (5-HT), regulate neural dynamics across multiple spatial and temporal scales and are implicated in the onset and progression of numerous neurological and psychiatric disorders [4–9]. Elucidating both transient and steady-state monoamine release patterns, and their corresponding effects on electrophysiological signaling, is critical for understanding the underlying pathophysiology. However, achieving stable, high-resolution, and reliable in vivo detection of both tonic and phasic neurotransmitter dynamics, while simultaneously recording electrical activity, remains limited by electrode materials and the long-term stability of the tissue–device interface.

This is an open access article under the terms of the Creative Commons Attribution License, which permits use, distribution and reproduction in any medium, provided the original work is properly cited.

© 2026 The Author(s). *Advanced Functional Materials* published by Wiley-VCH GmbH

Conventional silicon microelectrode arrays (MEAs) are widely used for neurophysiology [10–13]; however, standard metal recording sites (Au, Pt, Ir) exhibit intrinsically low sensitivity to monoamine neurotransmitters [14] and suffer from chronic performance degradation due to mechanical mismatch with soft brain tissue [15–19]. Penetration trauma, foreign-body responses, and glial encapsulation reduce neuronal proximity and progressively compromise long-term fidelity for both electrophysiological and neurochemical measurements [20–22]. Flexible polymer MEAs mitigate mechanical mismatch and improve chronic electrophysiological stability [23–27], but they typically still rely on metal sensing sites and thus do not resolve fundamental limitations in electrochemical monoamine detection.

Electroactive neurotransmitters can be detected with high sensitivity via electrochemical methods, particularly at carbon-based electrode surfaces [25, 28–31]. Two major strategies have emerged to integrate neurochemical sensing into MEAs. One approach directly incorporates carbon materials such as glassy carbon (GC) [32–34], graphene [35, 36], or boron-doped polycrystalline diamond (BDD) [37–39], into flexible substrates, providing fast electron-transfer kinetics, wide potential windows, and excellent electrochemical stability compatible with fast-scan cyclic voltammetry (FSCV) for phasic measurements. A second approach uses conducting polymer coatings (e.g., poly(3,4-ethylenedioxythiophene)(PEDOT)-based composites) with nanocarbon dopants to enhance sensitivity and electrochemical stability, enabling neurochemical detection using square-wave voltammetry (SWV) [32, 33, 40] and chronoamperometry [41, 42] alongside electrophysiological recording [41, 43]. These advances support dual-mode recording across brain regions, including selective functionalization of GC-MEAs that separates phasic FSCV measurements (uncoated GC sites) from tonic SWV measurements (PEDOT/CNT-coated sites) [33].

A central remaining challenge is resolving neurotransmitter dynamics across multiple timescales in vivo. FSCV is the established method for sub-second monitoring of phasic release, but the requirement of background-subtraction precludes accurate quantification of tonic levels [44–46]. Optimized SWV suppresses capacitive charging currents through differential sampling and enables direct in vivo measurement of basal neurotransmitter concentrations with second-scale resolution [32, 33, 40]. This indicates that specialized electrochemical strategies are required to resolve multi-timescale neurotransmitter dynamics. However, waveform optimization alone is insufficient; stable tonic detection depends on electrode materials that simultaneously promote efficient charge transfer, high sensitivity, and resistance to fouling in complex physiological environment. These needs motivate exploration of emerging electroactive materials platforms that can be integrated as robust, multifunctional coatings for neural interfaces.

MXenes are a family of 2D transition-metal carbides and nitrides with the general formula $M_{n+1}X_nT_x$ (n = 1–4), where M is an early transition metal, X is carbon or nitrogen, and T_x stands for surface terminations (e.g., O, OH, and F) [47, 48]. They are produced by selective etching of atomically thin metal layers from layered ceramics called MAX phases [49, 50]. Owing to their unique properties and tunable compositional and structural space, MXenes enable a wide range of applications [51–53]. While MXenes are most established in energy storage [53–55] and show strong industrial relevance in electromagnetic interference (EMI) shielding [56–58], they have more recently emerged as particularly promising functional materials for wearable sensors [59–61] and bioelectronics [62–64]. Their high electrical conductivity, mechanical flexibility, and chemically tunable surface functionality [65–67] make them exceptional candidates for multifunctional bioelectronic interfaces, enabling low-impedance, high signal-to-noise electrical coupling with biological tissues, including neural and cardiac interfaces [68–77].

Among these materials, titanium carbide ($Ti_3C_2T_x$) is particularly attractive for sensing applications due to its high electrical conductivity, large surface area, and abundant functional groups that enhance interactions with electroactive analytes [73]. In addition, $Ti_3C_2T_x$ disperses readily in aqueous media and can be processed into composite coatings [78–81]. Prior work has shown that $Ti_3C_2T_x$ incorporated into PEDOT: polystyrene sulfonate (PSS) improves electrochemical stability and electrocatalytic activity toward DA [82], while its hydrophilicity and reported antibiofouling behavior support integration at the neural interface [69]. Incorporation of $Ti_3C_2T_x$ MXene into neuroelectronic devices have also demonstrated to reduce impedance and baseline noise and improve signal quality relative to conventional gold microelectrodes [69].

Despite these advantages, $Ti_3C_2T_x$ MXene has not been established as a functional coating for in vivo electrochemical detection of tonic DA and 5-HT in the living brain. Here, we address this gap by developing $Ti_3C_2T_x$ MXene/PEDOT composite coatings as multifunctional interfaces for both GC and metal MEAs, enabling robust SWV monitoring of tonic DA and 5-HT alongside electrophysiological recording.

We first developed uniform $Ti_3C_2T_x$ MXene/PEDOT composite (MXene/PEDOT) coatings with controlled flake integration on GC-MEAs and systematically evaluated their electrochemical performance for tonic DA and 5-HT detection using SWV, including assessments of sensitivity, selectivity, electrochemical stability, and biofouling resistance. The optimized coatings were subsequently validated in vivo through implantation into distinct mouse brain regions, enabling reliable detection of DA (striatum), 5-HT (amygdala and prefrontal cortex), and simultaneous discrimination of DA and 5-HT (striatum). Because GC-MEAs have previously been demonstrated to support FSCV-based phasic neurotransmitter detection and electrophysiological recording, this platform uniquely enables multimodal, multi-timescale, and multi-analyte neural measurements. Finally, we extended the MXene/PEDOT-coating strategy to metal MEAs, demonstrating that $Ti_3C_2T_x$ similarly enables tonic neurotransmitter detection and electrophysiological recording. These results establish MXene modification as a broadly applicable strategy for transforming conventional metal microelectrodes into multimodal, multi-analyte neural interfaces.

16163028, 2026, 46, Downloaded from https://advanced.onlinelibrary.wiley.com/doi/10.1002/adfm.75402 by University Degli Studi Di Genova, Wiley Online Library on [28/06/2026]. See the Terms and Conditions (https://onlinelibrary.wiley.com/terms-and-conditions) on Wiley Online Library for rules of use; OA articles are governed by the applicable Creative Commons License

2 | Results

2.1 | Morphological and Electrochemical Characterization

Flexible GC-MEAs were successfully fabricated using a previously established photolithography process [32, 33], and their structural and electrochemical properties have been extensively characterized in our earlier work [32, 34]. By combining the electrochemical stability and monoamine sensitivity of GC microelectrodes with the conformability of thin-film flexible devices, GC-MEAs offer important advantages over stiff metal electrode silicon probes, including reduced tissue inflammation [32] and compatibility with FSCV [33, 38, 39], enabling multimodal sensing. However, extending GC-MEAs to multianalyte tonic detection requires advanced functional materials that enhance charge transfer, improve sensitivity, and mitigate fouling. MXenes represent a promising class of such materials: their high conductivity, hydrophilic surface terminations, and strong adhesion to carbon substrates make them well-suited as multifunctional coatings for next-generation neural interfaces [47, 49, 73]. In this work, we leverage an MXene/PEDOT composite coating to integrate tonic DA and serotonin 5-HT, individually and simultaneously, onto GC-MEAs that already support FSCV and electrophysiological recording.

MXene/PEDOT coating was electropolymerized directly onto the GC microelectrode surface. Optical microscopy confirmed the successful formation of a uniform, conformal MXene/PEDOT composite layer on the GC microelectrode surface (oval, ~2.5×10^3 μm^2), in clear contrast to the unmodified GC counterparts (Figure 1A). The MXene/PEDOT composite was deposited via chronoamperometry using a total charge of 75 mC cm^{-2}, an optimized parameter that provided the best balance of impedance reduction and charge transfer capacitance. This balance enabled reliable extraction of faradaic peaks by SWV, thereby enhancing neurotransmitter sensitivity for electrodes of this dimension.

High-resolution scanning electron microscopy (SEM) imaging (Figure 1B,C) revealed the presence of bright, lamellar MXene flakes embedded throughout the PEDOT matrix. These flakes exhibited the characteristic layered morphology of $Ti_3C_2T_x$ and appeared well integrated within the polymer network. Energy-dispersive X-ray spectroscopy (EDS) further supported this interpretation, with titanium (Ti), a signature element of the MXene phase, detected across the full electrode surface (Figure 1D–G). Regions containing visually prominent MXene flakes in the SEM micrographs corresponded to areas of intensified Ti signal in the elemental maps, confirming both successful incorporation and uniform spatial distribution of MXene within the electropolymerized composite coating (Figures S1B and S2B). The sulfur signal observed in the composite (Figure 1G; Figures S1E and S2E) is attributed to the thiophene units of PEDOT, confirming successful polymer growth and the presence of a continuous PEDOT matrix within the MXene/PEDOT coating.

These results, aligned with earlier findings [82], confirm that MXene participates as the operative dopant during EDOT electropolymerization and becomes stably integrated within the PEDOT matrix. The small quantity of PSS (1 mg PSS vs 16 mg MXene) served predominantly to stabilize the precursor mixture, while PEG promoted dispersion and suppressed premature precipitation.

Cyclic voltammograms of the GC microelectrodes before and after MXene/PEDOT coating (Figure 1H) show enhanced charge exchange between the electrode and electrolyte following coating, consistent with the increased effective area of the nanostructured layer. The charge storage capacity (CSC), calculated as the time integral of an entire CV cycle divided by the geometric area, increased from 1.47± 0.28 to 15.35 ± 3.05 mC cm^{-2} after coating, indicating an order of magnitude enhancement in electroactive surface area. Because an increase in CSC was expected a priori, a one-sided Wilcoxon signed-rank test (alternative hypothesis: median $\Delta CSC > 0$) was applied to the paired CSC differences (post − pre). All paired differences were positive, yielding W (Wilcoxon signed-rank test) = 15 and p-value = 0.031, confirming a statistically significant increase in CSC after MXene/PEDOT deposition.

Electrochemical impedance spectroscopy further supports the improved electrochemical performance of the coated electrodes (Figure 1I,J). The high surface area and enhanced conductivity of the MXene/PEDOT film produced a marked reduction in impedance across the entire measured frequency range. At 1 kHz, impedance decreased from 67.6 ± 4.5 to 10.9 ± 0.8 kΩ ($n = 5$), corresponding to an ~84% reduction. At 10 Hz, impedance decreased from 31.7 ± 5.8 MΩ to 205.1 ± 8.7 kΩ, corresponding to an ~99% reduction. These reductions were statistically significant at both frequencies (paired t-test, $p < 0.0001$), confirming improved electrode conductivity and charge-transfer properties. The phase angle response (Figure 1J) is consistent with these findings: the MXene/PEDOT-coated electrodes exhibit values closer to 90° at low frequencies, indicative of more ideal capacitive behavior, and both electrodes transition toward 0° (more resistive behavior) at higher frequencies.

Given the widespread use of PEDOT:PSS in bioelectronics and its well-established ability to reduce impedance and enhance charge storage [83–85], we employed it as a control to isolate the MXene-specific contribution (Figure 1H–J; Figure S3). Both CSC and impedance were evaluated for GC electrodes coated with PEDOT:PSS and MXene/PEDOT films electrochemically deposited under identical charge density conditions. For PEDOT:PSS, the CSC was 7.12 ± 1.26 mC cm^{-2}, approximately 54% lower than that of the MXene coatings. Although CSC values were higher for MXene/PEDOT in all paired samples, a paired two-sided Wilcoxon signed-rank test indicated that this difference did not reach statistical significance ($W = 15$, $p = 0.062$).

At 1 kHz, PEDOT:PSS-coated electrodes exhibited slightly lower impedance (8.95 ± 0.60 kΩ) than MXene/PEDOT-coated electrodes (10.77 ± 0.85 kΩ), although this difference was also not statistically significant ($W = 15$, $p = 0.062$). Additionally, paired comparisons using a two-sided Wilcoxon signed-rank test indicated no statistically significant difference across the frequency spectrum, consistent with their similar impedance profiles. Together, these results indicate that MXene incorporation consistently enhances charge storage relative to PEDOT:PSS, while differences in impedance remain modest under the tested conditions.

16163028, 2026, 46, Downloaded from https://advanced.onlinelibrary.wiley.com/doi/10.1002/adfm.75402 by University Degli Studi Di Genova, Wiley Online Library on [28/06/2026]. See the Terms and Conditions (https://onlinelibrary.wiley.com/terms-and-conditions) on Wiley Online Library for rules of use; OA articles are governed by the applicable Creative Commons License

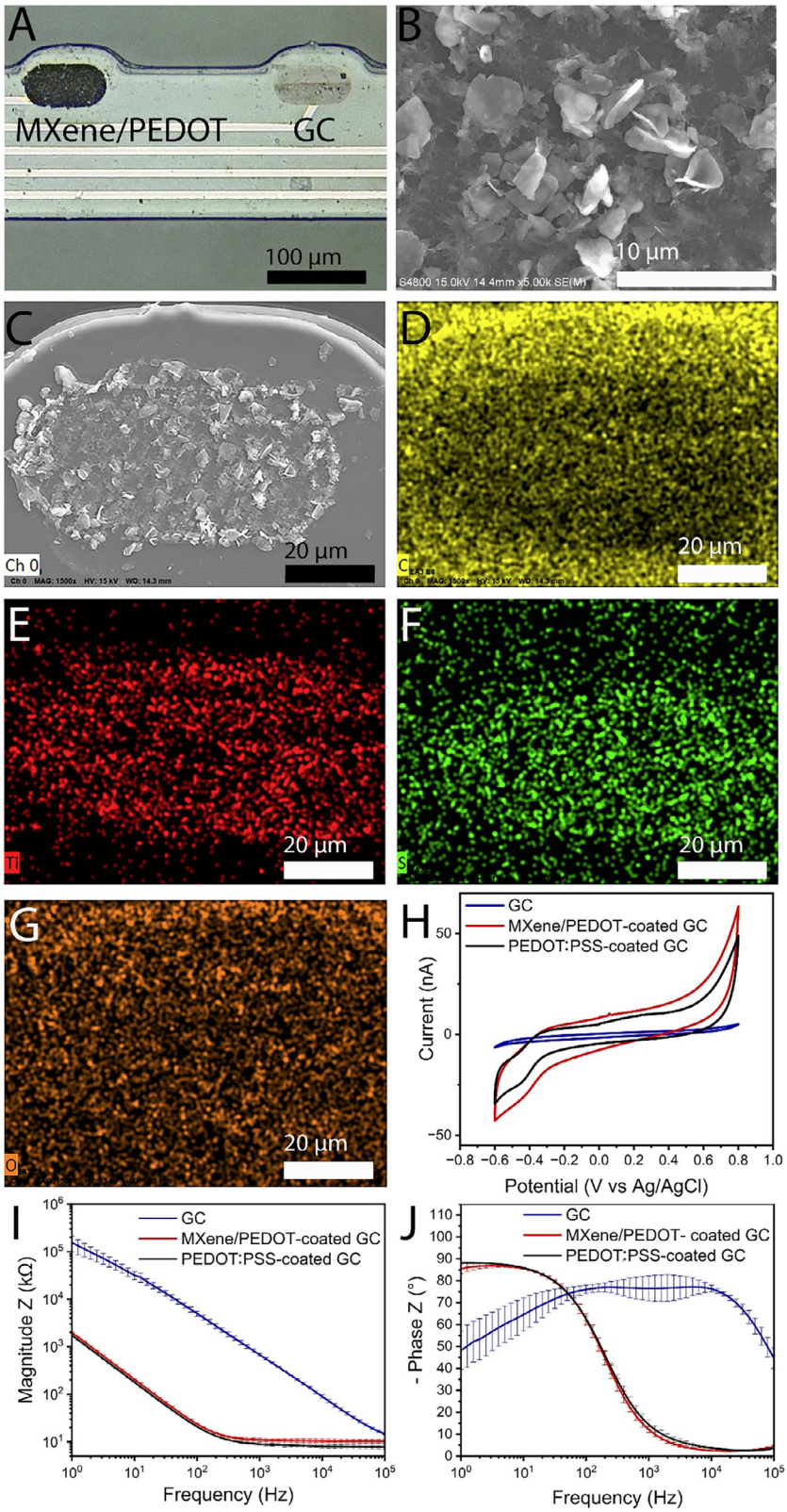

FIGURE 1 | GC-MEA characterization before and after MXene/PEDOT coating. (A) Optical microscopy images of oval-shaped microelectrodes ($\sim 2.5 \times 10^3$ µm^2), showing uniform MXene/PEDOT coverage and clear contrast between coated and uncoated GC microelectrodes (scale bar: 100 µm). (B) SEM images revealing MXene flakes embedded within the PEDOT matrix. (C–G) EDS elemental mapping confirming homogeneous Ti distribution, demonstrating successful MXene incorporation. Color legend: C (yellow, D), Ti (red, E), S (green, F), O (orange, G). (H) Cyclic voltammetry of uncoated (blue), MXene/PEDOT-coated (red) and PEDOT:PSS-coated GC electrodes showing increased electroactive surface area and enhanced charge-storage capability after coatings. (I) Electrochemical impedance spectra displaying reduced impedance across the entire frequency range for coated electrodes, indicating improved conductivity and charge transfer. (J) Phase-angle plots showing a more capacitive behavior at low frequencies after coating.

16163028, 2026, 46, Downloaded from https://advanced.onlinelibrary.wiley.com/doi/10.1002/adfm.75402 by University Degli Studi Di Genova, Wiley Online Library on [28/06/2026]. See the Terms and Conditions (https://onlinelibrary.wiley.com/terms-and-conditions) on Wiley Online Library for rules of use; OA articles are governed by the applicable Creative Commons License

Scanning electron microscopy (SEM) was used to investigate the surface morphology of the coatings (Figure S3). In contrast to the rough and porous morphology of the MXene/PEDOT coatings, which exhibit flake-like features characteristic of MXene embedded within the polymer matrix, PEDOT:PSS-coated electrodes display a relatively smooth and uniform surface consistent with a continuous polymer film. The nanostructured morphology of the MXene/PEDOT coatings provides increased effective surface area and a higher density of electroactive sites, likely contributing to the enhanced CSC. Additionally, MXene incorporation may introduce pseudocapacitive contributions and improved electronic pathways. While the less uniform conductive network may account for the slightly higher impedance relative to PEDOT:PSS, these findings highlight the advantage of MXene incorporation in substantially enhancing charge storage without notably compromising impedance.

2.2 | MXene/PEDOT for DA and 5-HT Square Wave Voltammetry Sensing

The intrinsic redox activity of electroactive neurotransmitters, including DA and 5-HT, enables their direct measurement using electrochemical techniques [86]. Here, we employ an optimized SWV waveform in combination with an MXene/PEDOT coating on GC-MEAs to detect tonic DA and 5-HT concentrations, as well as their simultaneous presence, both in vitro and in the mouse brain. Although MXenes, and in particular $Ti_3C_2T_x$ MXene, have shown strong promise for biosensing applications [87–90], their in vivo use remains largely unexplored. To our knowledge, this work represents the first use of a $Ti_3C_2T_x$ MXene/PEDOT coating on implantable microelectrode arrays for tonic multianalyte sensing.

By sampling and differencing forward and reverse currents, SWV minimizes capacitive charging currents and enhances faradaic sensitivity, making it well suited for tonic neurotransmitter detection. In our previous work, we developed separate SWV waveforms for DA [40] and 5-HT [32] detection to mitigate electrode fouling during 5-HT measurements. Specifically, for the 5-HT waveform, the lower potential limit was set to 0.15 V and held between scans to suppress fouling caused by quinone-imine electrochemical byproducts. However, this strategy precluded the simultaneous detection of DA and 5-HT.

In this study, leveraging the promising antifouling performance of MXene-based coatings and motivated by the need to evaluate their in vivo applicability, we developed a single SWV waveform capable of resolving both analytes. By systematically varying parameters known to influence voltammetric responses, including frequency, step potential, pulse amplitude, holding potential and time [91], we identified an optimized waveform that enabled dual-analyte detection. The optimal waveform consisted of a square wave with a 50 mV pulse amplitude, 5 mV step height, and 40 Hz frequency, scanned from −0.2 to 0.45 V, allowing clear discrimination of DA and 5-HT oxidation peaks.

The electrochemical performance of MXene/PEDOT-coated GC-MEAs for the detection of DA and 5-HT was first evaluated through in vitro calibration experiments conducted in 1× PBS. Electrode sensitivity was defined as the slope of the calibration curve obtained by plotting peak oxidation current as a function of analyte concentration (mean and SD, $n = 5$) over the range of 0.05 – 1 μM, corresponding to physiologically relevant concentrations (Figure 2A) [40, 92–97].

For DA, a well-defined oxidation peak was consistently observed at ∼0.11 V, with baseline-subtracted SWV showing a concentration-dependent increase in peak current (Figure 2B). Linear regression of the calibration curve confirmed excellent linearity ($R^2 = 0.9962$; Figure 2A), yielding a sensitivity of 2.46 ± 0.09 nA μM^{-1} and a limit of detection (LOD), calculated as 3σ/slope, of 9.6 ± 0.9 nM.

Similarly, 5-HT exhibited a distinct oxidation peak at ∼0.28 V, and baseline-subtracted SWV displayed a proportional increase in peak current with increasing concentration (Figure 2C). Linear calibration confirmed this behavior ($R^2 = 0.9933$; Figure 2A), with a sensitivity of 3.12 ± 0.15 nA μM^{-1} and a LOD of 4.7 ± 1.0 nM, demonstrating reliable detection across the tested concentration range.

The sensitivity achieved with the MXene/PEDOT coating is significantly higher than that of conventional carbon fiber electrodes (CFEs) [32, 40]. Although it is lower than that previously reported for PEDOT/CNT coatings, it remains sufficient to resolve in vivo–relevant concentrations with high resolution. This lower sensitivity is attributed to a reduced effective electroactive surface area relative to PEDOT/CNT, as reflected by the lower CSC (10 vs 93 ± 10 mC cm^{-2}) [32]. This difference is consistent with dopant size and geometry during electropolymerization: larger, 2D MXene nanosheets favor more compact PEDOT growth, whereas smaller, 1D CNT dopants promote higher nucleation density and a more porous morphology, increasing accessible area and sensitivity. Reduced capacitive charging associated with the more compact MXene/PEDOT morphology enhances SWV baseline stability, allowing low-amplitude faradaic signals to be resolved despite lower overall charge storage. This emphasizes that in SWV, optimal performance reflects a trade-off between charge storage capacity and faradaic signal resolvability, as excessive capacitive charging can degrade baseline stability and limit discrimination of low-amplitude redox peaks despite increased surface area.

Within the goal of this study to enable DA and 5-HT detection while mitigating electrochemical interference and biofouling, $Ti_3C_2T_x$ MXene therefore represents an attractive material to explore in vivo on implantable microelectrode arrays.

DA and 5-HT peaks are clearly well resolved and detected using a single SWV waveform. For each scan, DA and 5-HT signals were isolated from the non-faradaic background by subtraction of a modeled polynomial baseline, following previous established methods [40, 97]. A representative SWV trace and the corresponding baseline fits for 1 μM DA and 5-HT are shown in Figure 2D, while the background-subtracted waveforms are presented in Figure 2E.

The ability to simultaneously detect DA and 5-HT is highly significant due to their closely coupled roles in reward and decision making [98, 99], as well as in neurological disorders [100–102]. However, this capability remains challenging because

16163028, 2026, 46, Downloaded from https://advanced.onlinelibrary.wiley.com/doi/10.1002/adfm.75402 by University Degli Studi Di Genova, Wiley Online Library on [28/06/2026]. See the Terms and Conditions (https://onlinelibrary.wiley.com/terms-and-conditions) on Wiley Online Library for rules of use; OA articles are governed by the applicable Creative Commons License

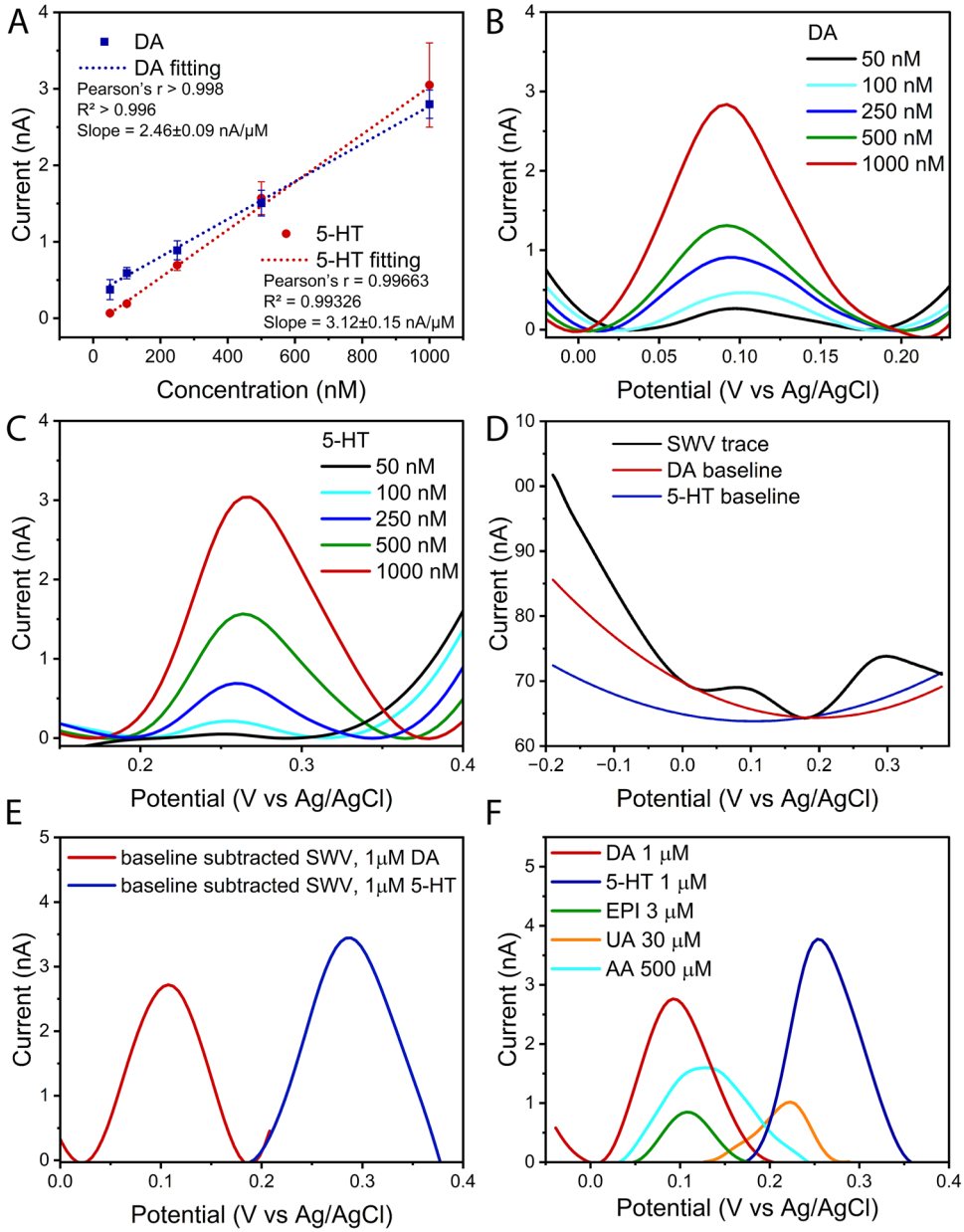

FIGURE 2 | In vitro SWV, calibration, and selectivity. (A) Calibration plots of peak current versus analyte concentration for DA and 5-HT, exhibiting linear responses (DA: $R^2 = 0.9962$, 5-HT: $R^2 = 0.993$) within the tested range, with sensitivities of 2.5 and 3 nA μM^{-1}, respectively. (B) Baseline subtracted SWVs for increasing DA concentrations (50 nM - 1 μM, $n = 5$ electrodes), showing a distinct oxidation peak around 0.11 V. (C) SWV responses for 5-HT under the same concentration range ($n = 5$), with oxidation peaks centered near 0.28 V. (D) Representative SWV response for simultaneous detection of 1 μM DA and 1 μM 5-HT. A second-order polynomial was used to model the background current separately within the potential regions of interest for DA and 5-HT. The polynomial fit for the DA peak is shown in red, and that for the 5-HT peak in blue. (E) Background subtraction using the polynomial fits reveals clear, concentration-dependent Gaussian peaks for DA and 5-HT. (F) Selectivity analysis against common electroactive interferents: epinephrine (EPI, 3 μM), ascorbic acid (AA, 500 μM), and uric acid (UA, 30 μM).

these neurotransmitters exhibit similar oxidation potentials using FSCV and conventional carbon-based microelectrodes [103, 104]. The clear separation observed here highlights the advantage of the present approach for effective dual-analyte resolution using a single waveform.

We next evaluated the selectivity of MXene/PEDOT-coated GC microelectrodes for DA and 5-HT in the presence of major neurochemical interferents, including 3 μM epinephrine (EPI), 30 μM uric acid (UA), and 500 μM ascorbic acid (AA). As described above, DA and 5-HT exhibit well-separated oxidation peaks at 0.10 and 0.28 V, respectively, while peaks corresponding to EPI (0.12 V), AA (0.14 V), and UA (0.23 V) were observed at their respective, relatively high concentrations, consistent with previous reports for PEDOT/CNT coatings (Figure 2F). Although partial overlap between DA, EPI, and AA is observed, the MXene/PEDOT electrodes exhibit substantially higher sensitivity toward DA compared to EPI and AA, despite the latter being tested at much higher concentrations. This selectivity is particularly relevant under physiological conditions, as DA is the

16163028, 2026, 46, Downloaded from https://advanced.onlinelibrary.wiley.com/doi/10.1002/adfm.75402 by University Degli Studi Di Genova, Wiley Online Library on [28/06/2026]. See the Terms and Conditions (https://onlinelibrary.wiley.com/terms-and-conditions) on Wiley Online Library for rules of use; OA articles are governed by the applicable Creative Commons License

predominant catecholamine in dopaminergic brain regions such as the striatum, where basal extracellular DA is typically in the 50–100 nM range [33, 40, 105, 106], whereas EPI is present at much lower and more regionally restricted concentrations in the central nervous system (highest in select hypothalamic nuclei) [107, 108]. Together, these results demonstrate that MXene/PEDOT coatings enable selective and reliable detection of DA and 5-HT in complex neurochemical environments.

2.3 | Stability to Electrochemical Fouling and Biofouling Experiments

Electrochemical sensors are susceptible to both electrochemical fouling and biofouling when used in vivo. Electrochemical fouling originates from the adsorption and electrochemical polymerization of redox-active species and their oxidation byproducts on the electrode surface, which can progressively block active sites and hinder electron transfer [109, 110]. Biofouling, on the other hand, is caused by the nonspecific adsorption of biomolecules forming a biological layer that limits analyte diffusion and degrades sensor performance [111, 112].

To evaluate the electrochemical fouling performance of the MXene/PEDOT coating upon exposure to DA and 5-HT, measurements were performed under continuous SWV scanning in the presence of 1 μM DA or 1 μM 5-HT for multiple days. Figure 3A presents a bar plot of DA peak currents measured over a period of up to 123 h (mean ± SD, $n = 5$). The electrodes consistently maintain reliable DA detection throughout this time window. Peak currents remain close to the initial value for most of the recording period, with only a gradual decrease observed at later time points. Even at 123 h, the reduction in DA current was limited to approximately 6% relative to the initial measurement, indicating minimal electrochemical fouling. Representative SWV curves recorded at selected time points, shown above the bar plot, displayed a consistent and well-defined DA oxidation peak.

Figure 3B presents a bar plot of 5-HT peak currents measured over a period of up to 42 h under continuous SWV scanning in presence of 1 μM 5-HT (mean ± SD, $n = 5$).

MXene/PEDOT-coated GC microelectrodes demonstrated robust and reproducible 5-HT detection over this extended time period. Peak currents remain stable during the first 10 h and then gradually decline at longer times. The decrease in signal remains modest, corresponding to a loss of ~9% at 20 h, ~11% at 25–32 h, and ~22% at 42 h relative to the initial value. Notably, even after 42 h of continuous scanning and exposure, the microelectrodes retained approximately 78% of the original 5-HT signal. Representative SWV curves recorded at selected time points displayed a well-defined and stable oxidation peak, further confirming the sustained electrochemical performance. In addition, electrochemical impedance spectra recorded at different time points showed only minimal variation across the entire frequency range, confirming the stability of the electrode interface under prolonged SWV scanning (Figure S4A).

The shorter operational lifetime and the higher signal loss observed for 5-HT compared to DA is likely due to its higher susceptibility to electrochemical fouling. Electrochemical detection

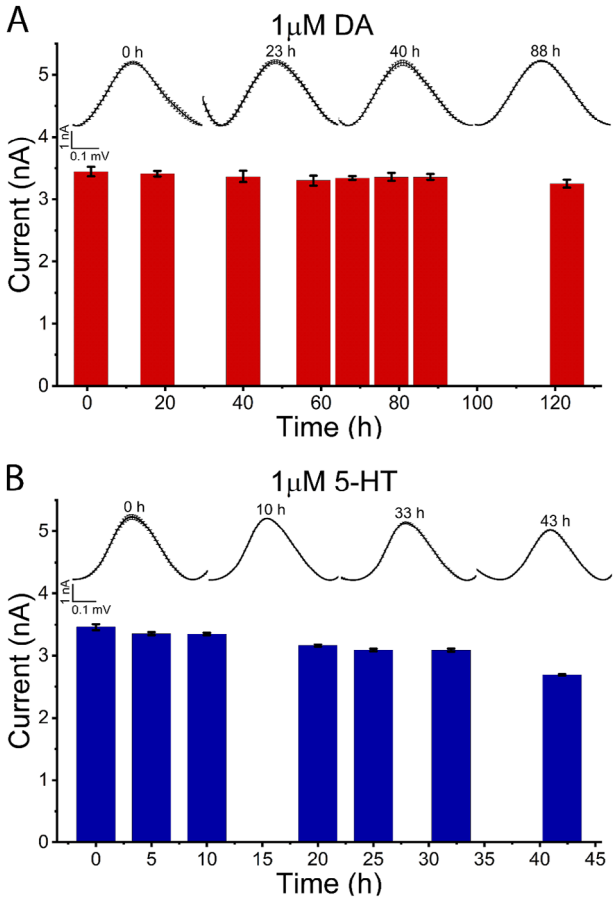

FIGURE 3 | Electrochemical fouling assessment in presence of 1 μM DA/5-HT. (A) DA sensing stability over continuous SWV scanning in presence of 1 μM DA for up to 123 h. Representative SWV curves at selected time points are shown above the bar plot. (B) 5-HT sensing stability in presence of 1 μM 5-HT over 43 h of continuous SWV scanning. Representative SWV curves at selected time points are shown above the bar plot. (A, B) Data are presented as mean ± SD ($n = 5$).

of 5-HT is particularly challenging because oxidation generates highly reactive intermediates and byproducts, such as carbocation species and dimers, that adsorb irreversibly on the electrode surface, leading to progressive surface fouling and loss of sensitivity [113–115]. This phenomenon underscores the critical role of electrode surface properties and material selection in mitigating fouling and preserving sensor performance. Notably, the DA and 5-HT concentrations used in these fouling tests (1 μM) are higher than tonic physiological levels, thereby providing a conservative, worst-case assessment of the long-term stability of the coating. Given the high fouling susceptibility of 5-HT, these results represent a substantial improvement over the current state of the art. To the best of our knowledge, this is the longest continuous electrochemical fouling test reported for both DA and 5-HT under constant potential scanning in the presence of a high analyte concentration (1 μM). Most previously reported fouling tests were performed only for a few hours [37, 115, 116] to a maximum of 24 h [117–119] and/or at lower analyte concentrations [38, 117, 118]. As a direct control, we investigated the fouling behavior of PEDOT:PSS coatings using the waveform optimized in this manuscript under continuous SWV scanning in the presence of 1 μM 5-HT. We observed the rapid formation of a secondary peak, most likely

16163028, 2026, 46, Downloaded from https://advanced.onlinelibrary.wiley.com/doi/10.1002/adfm.75402 by University Degli Studi Di Genova, Wiley Online Library on [28/06/2026]. See the Terms and Conditions (https://onlinelibrary.wiley.com/terms-and-conditions) on Wiley Online Library for rules of use; OA articles are governed by the applicable Creative Commons License

associated with the formation and accumulation of oxidation byproducts from the serotonin reaction [113–115]. In particular, a quinoneimine byproduct has previously been reported to form in 5-HT-rich environments at around 0 V and to contribute significantly to electrode fouling shortly after 5-HT exposure [120]. Figure S5A,B capture the progressive emergence and growth of this secondary peak over the first 25 min. Concomitantly, we observed a decrease in peak amplitude of approximately 33% after 1 h and 50% after 5 h, along with progressive peak broadening in the SWV response (Figure S5C). Such broadening is commonly associated with slower electron transfer kinetics and increased interfacial heterogeneity, further supporting electrode fouling [121].

The incorporation of $Ti_3C_2T_x$ MXene may contribute to the observed antifouling behavior, as its polar surface terminations (–O/–OH/–F) impart high hydrophilicity and have been associated with reduced nonspecific adsorption, while its high electronic conductivity and accessible surface area are widely leveraged to sustain electrochemical activity during prolonged electrochemical measurements and sensing [71, 122–125]. In addition to the material properties of the MXene/PEDOT interface, further reductions in electrochemical fouling could potentially be achieved through waveform optimization. For example, waveforms that initiate scanning at higher potentials and maintain a holding potential above 0.05 V have been shown to minimize polymerization of reactive oxidation byproducts, such as quinoneimine species, thereby limiting electrochemical fouling [32, 120, 126]. However, implementing such waveforms would preclude simultaneous detection of DA and 5-HT on the same electrode, highlighting a trade-off between maximal antifouling performance and multianalyte neurotransmitter sensing.

In addition to electrochemical fouling, biofouling was evaluated to assess electrode performance under simulated physiological conditions. MXene/PEDOT-coated GC-MEAs were immersed in a 40 g L^{-1} bovine serum albumin (BSA) solution for up to 10 h, after which sensitivity toward 5-HT, the neurotransmitter most susceptible to fouling, was evaluated at selected time points. BSA is a globular, water-soluble protein derived from bovine blood serum and is widely used as an in vitro model for biofouling in electrochemical sensors and biomaterial studies [43, 125, 127–129]. Albumin is the most abundant protein in blood plasma and extracellular fluids, typically present at concentrations of ~35–50 g L^{-1} and accounting for approximately 50%–60% of total plasma protein, making BSA exposure a physiologically relevant fouling challenge [129, 130]. Protein adsorption occurs rapidly when implantable electrodes contact biological fluids and can substantially alter interfacial properties [131]. In particular, the formation of adsorbed protein layers can impede electron transfer, increase charge-transfer resistance and interfacial impedance, and ultimately degrade electrochemical sensor sensitivity and stability [131, 132]. Consequently, exposure to concentrated BSA solutions provides a relevant and widely adopted model for evaluating resistance to biofouling and the ability of electrode coatings to maintain electrochemical functionality in biologically relevant environments.

SWV was performed using MXene/PEDOT-coated GC-MEAs after immersion in 40 g L^{-1} BSA for 0, 1, 7, and 10 h at 37°C. Figure 4A shows the corresponding 5-HT peak currents over time ($n = 6$, mean ± SD). The MXene/PEDOT-coated microelectrodes maintained robust and reproducible 5-HT detection throughout the exposure period, with no appreciable change in the 1 µM 5-HT oxidation peak across any of the time points. Representative SWV traces acquired at selected time points are shown above the bar plot.

After 10 h of BSA immersion, 1 µM 5-HT was measured simultaneously with 1 µM DA. Two well-resolved oxidation peaks corresponding to DA and 5-HT were observed, demonstrating that the sensors retained both sensitivity and analyte discrimination even after prolonged biofouling stress (Figure 4B). Electrochemical impedance spectra of MXene/PEDOT-coated GC-MEAs recorded at different time points exhibited only modest variations across the entire frequency range, further confirming the stability of the electrode interface (Figure S4B).

Notably, SEM imaging (Figure 4; Figures S6–S11) revealed no obvious morphological differences between control and biofouled samples. Consistent with this, corresponding EDS maps indicate that the distribution of key elements, including Ti (from the MXene phase) and S (associated with the thiophene groups of PEDOT), is preserved after biofouling, suggesting that fouling does not significantly alter the structural or compositional integrity of the coating.

2.4 | In Vivo Sensing

The in vivo performance of MXene/PEDOT-coated GC-MEAs for the detection of tonic 5-HT, tonic DA, and their simultaneous co-detection was evaluated through acute experiments conducted in different brain regions of isoflurane-anesthetized mice.

Specifically, DA detection was validated in the striatum, 5-HT detection in the amygdala and prefrontal cortex, and simultaneous DA and 5-HT co-detection in the striatum. The flexible MEAs were implanted into the mouse brain using a 50 µm tungsten wire inserted through the anchor hole at the shank tip and removed immediately after implantation, following our previously reported insertion method [32, 33, 43].

Following insertion into the striatum, tonic DA levels were detected using the SWV waveform. In vivo SWV measurements revealed a clear DA oxidation peak at ~0.12 V, as shown in Figure 5A, which presents average baseline-subtracted SWV collected from three mice. Baseline DA concentrations were estimated to be approximately 99 ± 29 nM (mean ± SEM, n = 4 mice 5 recording sites) based on a pre-established calibration curve. This concentration is consistent with previously reported tonic extracellular DA levels in the striatum under anesthetized conditions, supporting the physiological relevance of the measurements and confirming that the SWV waveform and electrode sensitivity are sufficient to resolve basal DA concentrations in vivo [33, 40, 94, 95, 133]. After recording basal levels for 10 min, to validate the chemical specificity of our measurements, mice were administered raclopride (2 mg kg^{-1}), a selective D2 receptor antagonist, together with nomifensine (20 mg kg^{-1}), a DA reuptake inhibitor. This pharmacological manipulation is expected to elevate extracellular DA by blocking D2 autoreceptor-mediated negative feedback on DA release and inhibiting DA

16163028, 2026, 46, Downloaded from https://advanced.onlinelibrary.wiley.com/doi/10.1002/adfm.75402 by University Degli Studi Di Genova, Wiley Online Library on [28/06/2026]. See the Terms and Conditions (https://onlinelibrary.wiley.com/terms-and-conditions) on Wiley Online Library for rules of use; OA articles are governed by the applicable Creative Commons License

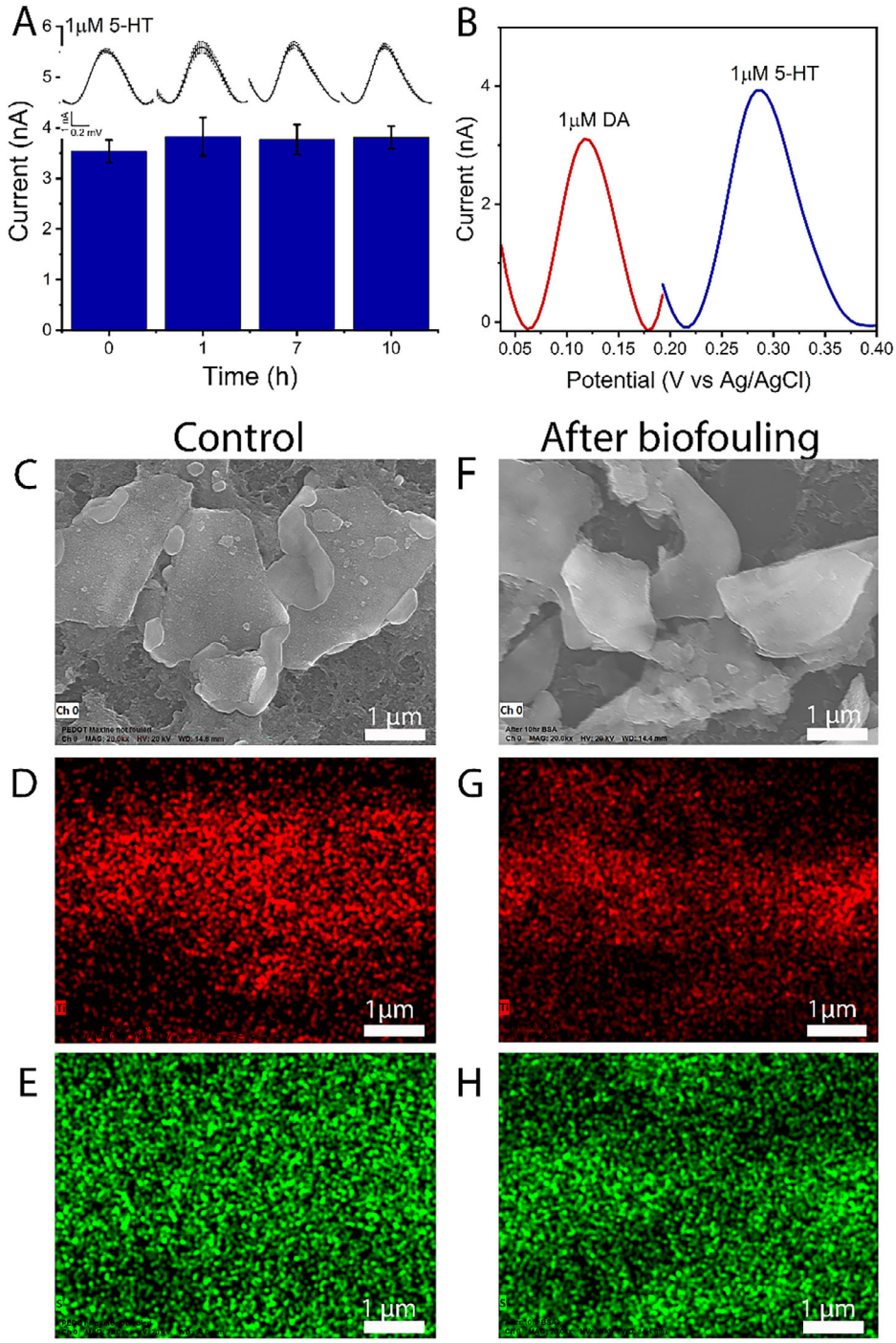

FIGURE 4 | Biofouling assessment over 10 h in 0.4 mg mL^{-1} BSA at 37°C. (A) SWV peak current responses to 1 μM 5-HT at MXene/PEDOT-coated electrodes following immersion in 40 g L^{-1} BSA for 0, 1, 7, and 10 h, demonstrating signal stability and resistance to biofouling. Representative SWV traces are shown above the corresponding bar plot. Data are presented as mean ± SD ($n = 6$); (B) SWV recorded after 10 h of BSA exposure following the addition of 1 μMM DA to 1 μM 5-HT, showing two well-resolved oxidation peaks and preserved analyte selectivity under fouling conditions. (C–H) SEM images and corresponding EDS maps of titanium (red) and sulfur (green) for MXene/PEDOT-coated electrodes: control (not subjected to fouling, C–E) and after biofouling (10 h in 0.4 mg mL^{-1} BSA at 37°C, (F–H). See also Figures S6–S11.

reuptake via dopamine transporter, while also engaging postsynaptic D2 receptors [92, 134–136]. 1 h after administration, DA concentrations increased to 906 ± 87 nM. Figure 5B shows a representative example of the time-dependent changes in DA concentration following drug administration, with DA levels rising steadily and reaching a maximum at ~1 h post-injection.

For 5-HT, multiple brain regions were investigated. Following insertion into the amygdala, tonic 5-HT levels were measured using the SWV waveform. In vivo SWV measurements revealed a well-defined 5-HT oxidation peak centered at ~0.28 V (Figure 5C), corresponding to a basal extracellular concentration of 20 ± 7 nM (mean ± SEM, $n = 2$) based on the pre-established

16163028, 2026, 46, Downloaded from https://advanced.onlinelibrary.wiley.com/doi/10.1002/adfm.75402 by University Degli Studi Di Genova, Wiley Online Library on [28/06/2026]. See the Terms and Conditions (https://onlinelibrary.wiley.com/terms-and-conditions) on Wiley Online Library for rules of use; OA articles are governed by the applicable Creative Commons License

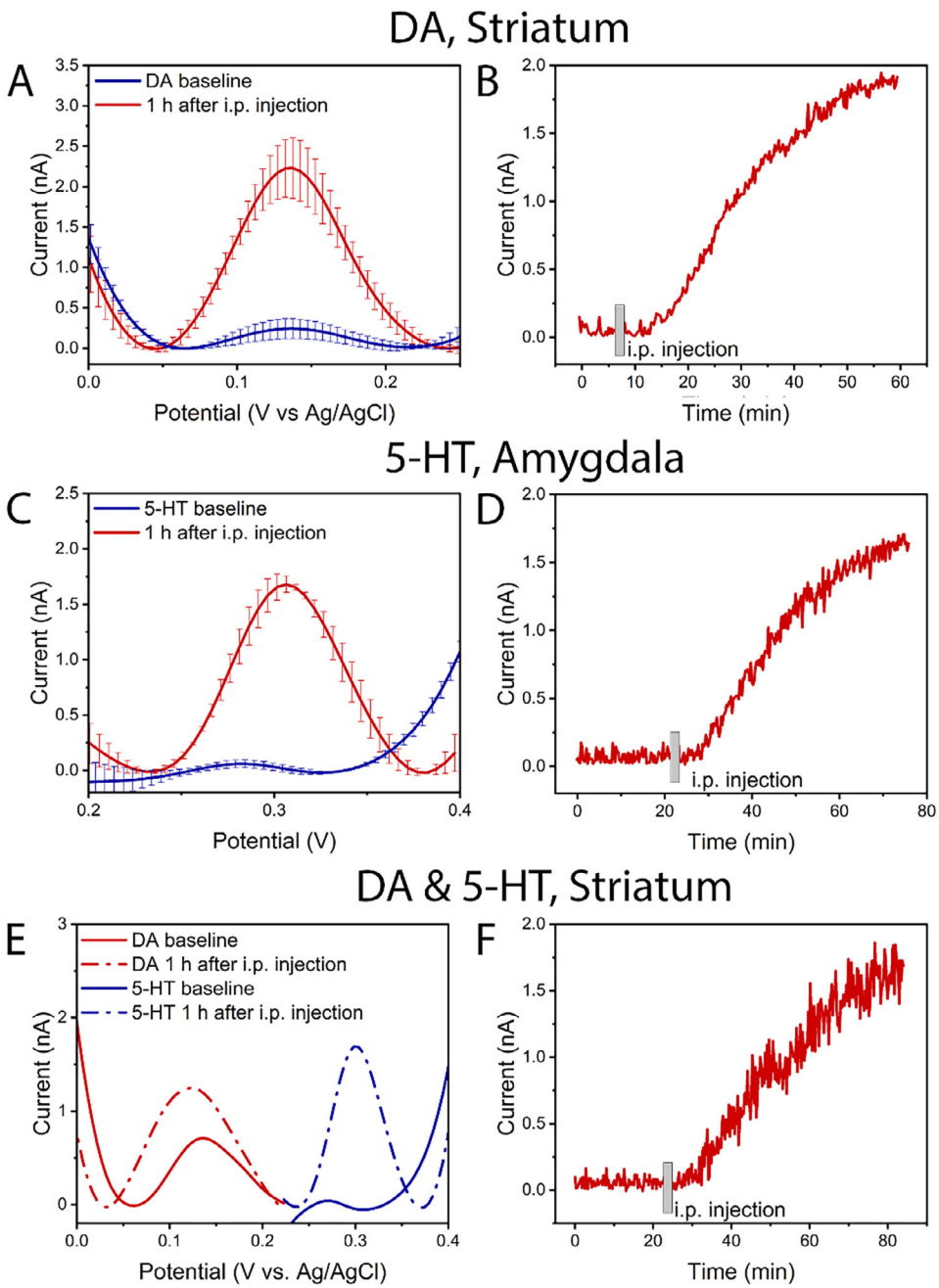

FIGURE 5 | In vivo SWV detection of DA and 5-HT in mouse brain. (A) SWV recordings in the striatum at baseline (blue) and 1 h after raclopride + nomifensine (red), showing an increased DA oxidation peak at ~0.15 V. (B) Time-dependent evolution of the DA peak current, displaying a progressive rise after drug injection (green bar). (C) SWV responses in the amygdala before and 1 h after carbidopa + 5-HTP, revealing a clear 5-HT oxidation peak at ~0.28 V. (D) Time course of the 5-HT peak current showing gradual increase post-injection. (E) Simultaneous detection of DA and 5-HT in the striatum: overlaid SWV traces at baseline and 1 h after carbidopa + 5-HTP show distinct oxidation peaks (~0.1 V for DA, ~0.28 V for 5-HT). (F) Temporal profile of 5-HT peak currents recorded under the same conditions.

5-HT calibration sensitivity. This basal 5-HT concentration falls within the lower range of values reported for tonic extracellular 5-HT in vivo [96, 97, 137]. The ability to resolve these low basal concentrations highlights the sensitivity of the MXene/PEDOT-coated microelectrodes for in vivo 5-HT detection. To confirm that the recorded electrochemical signal corresponded to 5-HT, its concentration was selectively elevated pharmacologically. Mice were i.p. administered carbidopa (25 mg kg^{-1}) and 5-hydroxytryptophan (5-HTP; 200 mg kg^{-1}), which resulted in a marked increase in extracellular 5-HT. The combined administration of 5-hydroxytryptophan (5-HTP) and carbidopa is a well-established pharmacological strategy to selectively elevate brain serotonin (5-HT) and has been widely used to validate in vivo electrochemical 5-HT measurements. 5-Hydroxytryptophan (5-HTP), the immediate metabolic precursor of 5-HT, readily crosses the blood–brain barrier (BBB) and is converted to 5-HT by aromatic L-amino acid decarboxylase (AADC). Co-administration of carbidopa, a peripheral AADC inhibitor that

16163028, 2026, 46, Downloaded from https://advanced.onlinelibrary.wiley.com/doi/10.1002/adfm.75402 by University Degli Studi Di Genova, Wiley Online Library on [28/06/2026]. See the Terms and Conditions (https://onlinelibrary.wiley.com/terms-and-conditions) on Wiley Online Library for rules of use; OA articles are governed by the applicable Creative Commons License

does not cross the BBB, suppresses peripheral 5-HT synthesis and increases the availability of 5-HTP for central conversion, resulting in a robust and selective elevation of brain 5-HT [103, 138, 139]. In this study, this pharmacological manipulation is not intended to recapitulate physiological 5-HT release, but rather to validate analyte identity and sensor selectivity under in vivo conditions. Following drug administration, 5-HT concentrations rose to approximately 560 ± 14 nM at 1 h post-injection. Figure 5D shows a representative example of the time-dependent changes in 5-HT concentration following drug administration. Notably, a progressive anodic shift in the 5-HT oxidation potential peak was observed, from ∼0.28 V at baseline to ∼0.32 V after drug administration (Figure S12; Figure 5C). Similar peak shifts have been reported during in vivo 5-HT measurements and may reflect alterations in the local chemical environment. Because 5-HT oxidation is proton-coupled, local pH variations, potentially induced by 5-HTP administration, can shift the oxidation potential to more positive values, consistent with the observed anodic displacement [140, 141].

In the prefrontal cortex (PFC), basal 5-HT levels were not reliably detected (Figure S13A), likely reflecting the lower extracellular concentrations in this region. However, following administration of carbidopa (25 mg kg^{-1}) and 5-HTP (200 mg kg^{-1}), 5-HT levels increased progressively over time, enabling clear detection and tracking of the pharmacologically evoked response (Figure S13B).

Finally, to enable simultaneous monitoring of DA and 5-HT, measurements were performed in the striatum, a brain region characterized by high extracellular DA levels and comparatively lower 5-HT concentrations. In this region, basal DA was readily detected, whereas basal 5-HT was below the detection limit (Figure 5 E). Following administration of carbidopa and 5-HTP, extracellular 5-HT levels increased markedly, reaching approximately 550 nM after 1 h from the injection (Figure 5 F). Although these pharmacological agents primarily target serotonergic pathways, an increase in DA concentration was also observed, with levels rising to approximately 500 nM. Although the pharmacological intervention selectively elevates 5-HT, the increase in DA levels is consistent with established serotonergic modulation of dopaminergic transmission in the striatum [142–144].

To assess electrode integrity and functionality throughout the in vivo experiments, impedance spectroscopy was performed under three conditions: in vitro in PBS prior to implantation, in vivo immediately after implantation in the brain, and in vitro in PBS following explantation (Figure S14). Impedance values were higher in vivo, consistent with the greater resistive and capacitive properties of brain tissue compared with PBS. Importantly, post-implantation impedance measurements in PBS showed only a slight increase relative to pre-implantation values, likely reflecting partial encapsulation of the MXene/PEDOT-coated GC-MEAs by biological material (e.g., blood) during explantation. These results indicate that the MEAs retained their electrochemical functionality and that the MXene/PEDOT coating did not delaminate during implantation.

Furthermore, because administration of carbidopa and 5-HTP produced sustained elevations of both 5-HT and DA in vivo for several hours, this drug-induced chemical environment enabled simultaneous assessment of electrochemical and biological fouling during continuous SWV scanning under physiologically relevant conditions. As shown in a representative example (Figure 6A), in vivo SWV recordings obtained with MXene/PEDOT-coated GC microelectrodes exhibited a stable pre-injection baseline followed by a sustained increase in the 5-HT current after i.p. administration, with the 5-HT oxidation peak remaining well defined throughout the ∼3.5-h recording period for both the analyte (Figure 6A inset). Impedance spectra acquired at implantation and after 210 min were largely superimposable, indicating that the electrode–tissue interface remained electrochemically stable over this acute timescale, with no evidence of biofouling or electrochemical fouling (Figure 6B).

2.5 | MXene/PEDOT Coated Platinum MEAs for Electrochemical Sensing and Electrophysiological Recording

Finally, we extended the MXene/PEDOT coating strategy to platinum (Pt)-MEAs with 700 μm^2 recording sites, demonstrating that $Ti_3C_2T_x$ MXene similarly enables tonic neurotransmitter detection on electrodes traditionally used exclusively for electrophysiological recordings [145, 146]. MXene/PEDOT functions as a transduction layer that enables electrochemical neurotransmitter sensitivity on metal electrodes that would otherwise be limited to electrical recording, as conventional electrode materials (e.g., Au, Pt, Ir) exhibit limited sensitivity for electrochemical neurotransmitter detection. Because conductive polymer composites can be deposited onto a wide range of conductive substrates, this modification strategy is readily applicable to commercially available metal MEAs, providing a practical route toward broadly accessible, multimodal, and multi-analyte neural interfaces.

Flexible Pt-MEAs were successfully fabricated using a previously established photolithography process [43, 147]. MXene/PEDOT was then electropolymerized directly onto the Pt sites. The composite was deposited by chronoamperometry to a total charge of 100 mC cm^{-2}, an optimized condition that reduced impedance while maintaining charge-transfer capacitance compatible with reliable faradaic peak extraction by SWV at this electrode size. Structural and compositional analyses confirmed successful composite formation (Figure 7A–F). Optical microscopy confirmed a uniform, conformal coating on the 30 µm in diameter Pt recording site (Figure 7A). High-resolution SEM images revealed a porous coating containing bright, lamellar features consistent with embedded MXene flakes (Figure 7B; Figures S15 and S16). EDS mapping showed Ti distributed across the electrode surface (MXene signature; Figure 7C) along with accompanying elemental signals consistent with the composite coating (Figure 7D–F; Figures S15 and S16), while the sulfur signal supported the presence of a continuous PEDOT matrix (Figure 7F).

Following deposition, impedance decreased across 10–10^4 Hz (Figure 7G), with magnitude impedance at 10 Hz reduced from 4.3 ± 1.0 MΩ to 841 ± 83 kΩ and at 1 kHz reduced from 141 ± 15.8 to 40 ± 6.5 kΩ (n = 5, paired t-test, $p < 0.0001$). The phase response was also shifted toward more capacitive behavior over relevant frequencies (Figure 7H), consistent with increased effective electrochemical surface area and enhanced charge transfer.

16163028, 2026, 46, Downloaded from https://advanced.onlinelibrary.wiley.com/doi/10.1002/adfm.75402 by University Degli Studi Di Genova, Wiley Online Library on [28/06/2026]. See the Terms and Conditions (https://onlinelibrary.wiley.com/terms-and-conditions) on Wiley Online Library for rules of use; OA articles are governed by the applicable Creative Commons License

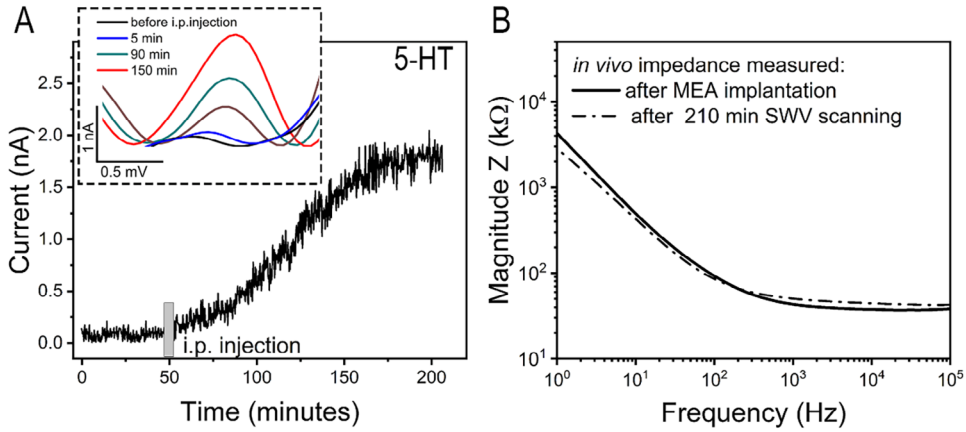

FIGURE 6 | Fouling in vivo. (A) 5-HT current recorded with an MXene/PEDOT-coated GC microelectrode over ~210 min. The gray bar indicates the time of i.p. injection. After a stable baseline, the current gradually increases, consistent with rising 5-HT levels. Inset: SWV responses (before injection and at selected times post-injection) showing a progressive increase in the 5-HT oxidation peak amplitude that shifts on the right; (B) Impedance spectra of the same microelectrode measured in the mouse brain immediately after implantation (solid line) and after 210 min of continuous SWV scanning (dashed line).

As a proof of concept for neurochemical sensing, MXene/PEDOT-coated Pt-MEAs enabled sensitive SWV detection of DA (0.93 ± 0.04 nA/μM) and 5-HT (1.20 ± 0.02 nA/μM) in 1× PBS over 50 nM – 1 μM (Figure 7I, L; Figure S17A), producing a well-defined oxidation peak near 0.1 and 0.28 V respectively. Using the same waveform, the electrodes also supported separable detection of DA and 5-HT, with distinct oxidation peaks (DA ~0.10 V; 5-HT ~0.28 V) (Figure S17B), demonstrating feasibility for multi-analyte sensing on metal MEA platforms.

Sensitivity decreases by ~2.6-fold for both DA and 5-HT compared to the larger GC electrodes (3.5-fold greater geometric area), consistent with the reduction in electroactive surface. Nevertheless, the microelectrodes retain a similar measurable concentration range within physiologically relevant levels, demonstrating the strong potential of electrode miniaturization for high-resolution electrochemical sensing. Notably, coating thickness must be tuned for each substrate and geometry to optimize SWV performance by balancing conductivity, sensitivity, and background (capacitive) currents, and can be precisely controlled by adjusting the charge density applied during deposition.

To demonstrate that the sensitivity of Pt-MEAs is sufficient for simultaneous in vivo monitoring of DA and 5-HT, we implanted MXene/PEDOT-coated Pt-MEAs into the mouse striatum, using the same procedure previously employed with MXene/PEDOT-coated GC-MEAs. After insertion, tonic DA and 5-HT levels were detected using the SWV waveform (Figure 8A). Following administration of carbidopa and 5-HTP, extracellular 5-HT levels increased markedly, reaching ~580 nM after 1 h (Figure 8A, B) and continuing to rise to ~800 nM after 85 min (Figure 8B). In this study, the pharmacological manipulation was intended to induce a robust, artificial increase in extracellular 5-HT, rather than to mimic physiological tonic dynamics, and was used primarily to validate analyte identity and sensor selectivity in vivo. Consistent with what was previously observed using MXene/PEDOT-coated GC-MEAs, DA levels also increased to ~500 nM from a basal level of ~95 nM, reflecting serotonergic modulation of dopaminergic signaling [142–144].

MXene/PEDOT-coated Pt MEAs also supported simultaneous electrophysiological recording in vivo, capturing spontaneous neuronal spiking activity in mouse somatosensory cortex (Figure 8C,D). Representative raw traces showed well-resolved spike events with peak-to-peak amplitudes of approximately −150 to +50 μV (Figure 8C), consistent with expectations for microelectrodes of similar size [43, 148]. Although low-frequency biological and motion-related noise was present, spike waveforms remained clearly distinguishable from baseline fluctuations.

Principal component analysis (PCA) was used for feature extraction, followed by k-mean clustering for spike sorting which isolated a dominant single-unit cluster with minimal multiunit contamination (Figure 8D).

To evaluate whether MXene/PEDOT-coated electrodes not only enable electrochemical sensing but also improve signal quality compared to uncoated electrodes, as previously demonstrated for PEDOT:PSS [149, 150] and other low-impedance conductive polymer and composite coatings [151–153], we measured the signal-to-noise ratio (SNR) of both coated and uncoated 30 μm diameter electrodes under controlled saline conditions and during in vivo recordings.

In saline, MXene/PEDOT-coated electrodes exhibited a significantly higher SNR compared to uncoated electrodes (Mann–Whitney U-test, $p < 0.01$), corresponding to approximately a twofold increase from 5.25 ± 0.20 to 11.29 ± 2.02 (Table S1). This enhancement is in line with the well-established electrochemical properties of PEDOT-based materials, including reduced impedance and increased effective surface area, which improve charge transfer and reduce thermal noise [150–152].

In vivo recordings showed a similar increase in SNR, with coated electrodes yielding higher values (9.49 ± 1.89) than uncoated electrodes (5.38 ± 0.23). These results support the conclusion that MXene/PEDOT coatings not only enable neurochemical sensing performance but also enhance electrophysiological

16163028, 2026, 46, Downloaded from https://advanced.onlinelibrary.wiley.com/doi/10.1002/adfm.75402 by University Degli Studi Di Genova, Wiley Online Library on [28/06/2026]. See the Terms and Conditions (https://onlinelibrary.wiley.com/terms-and-conditions) on Wiley Online Library for rules of use; OA articles are governed by the applicable Creative Commons License

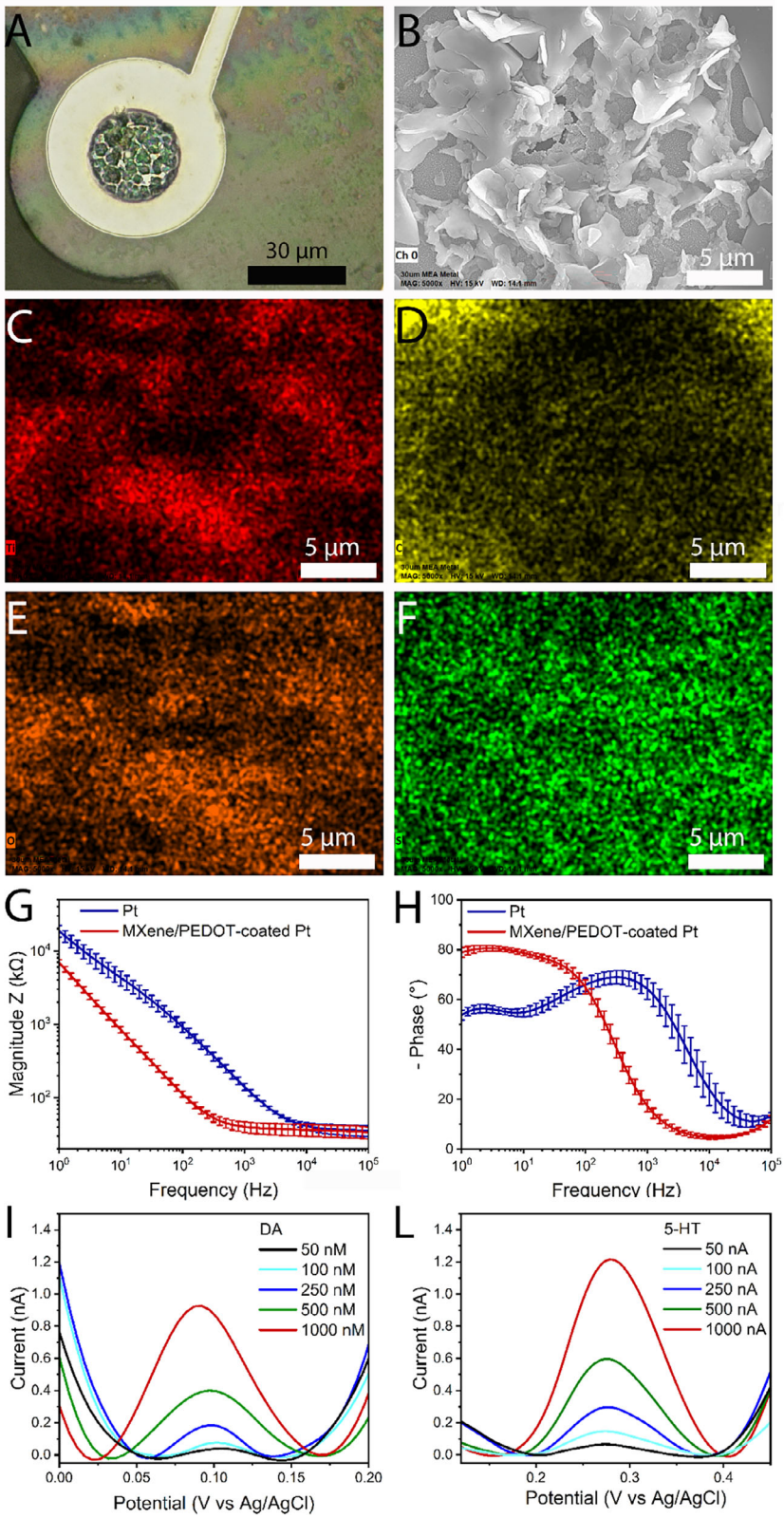

FIGURE 7 | Platinum MEA characterization before and after MXene/PEDOT coating. (A) Optical image of a MXene/PEDOT-coated Pt microelectrodes (30 µm in diameter). (B) SEM images revealing MXene flakes embedded within the PEDOT matrix. (C-F) EDS elemental mapping confirming homogeneous Ti distribution, demonstrating successful MXene incorporation. Color legend: Ti (red, C), C (yellow, D), O (orange, E), S (green, F). (G) Electrochemical impedance (magnitude) spectra displaying reduced impedance across the entire frequency range for coated electrodes, indicating improved conductivity and charge transfer. (H) Phase-angle plots show a more capacitive behavior at low frequencies after coating. (I) Baseline subtracted SWVs for increasing DA concentrations (50 nM–1 µM) showing a distinct oxidation peak around 0.1 V. (L) Baseline subtracted SWVs for increasing 5-HT concentrations (50 n–1 µM) showing a distinct oxidation peak around 0.28 V.

16163028, 2026, 46, Downloaded from https://advanced.onlinelibrary.wiley.com/doi/10.1002/adfm.75402 by University Degli Studi Di Genova, Wiley Online Library on [28/06/2026]. See the Terms and Conditions (https://onlinelibrary.wiley.com/terms-and-conditions) on Wiley Online Library for rules of use; OA articles are governed by the applicable Creative Commons License

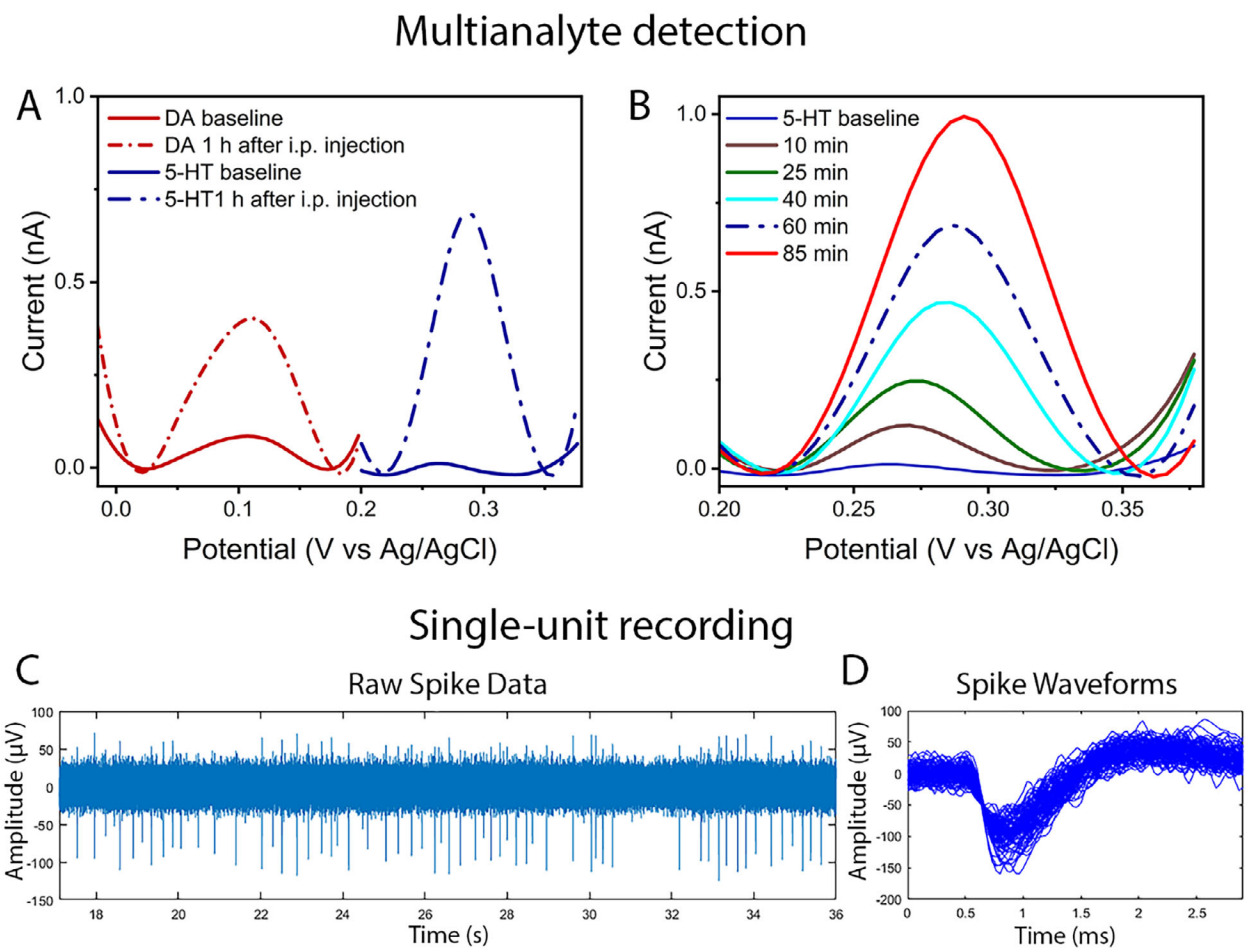

FIGURE 8 | Multianalyte (DA and 5-HT) detection and Single-unit recordings from MXene/PEDOT-coated Pt MEAs. (A) Simultaneous detection of DA and 5-HT in the mouse striatum: overlaid SWV traces at baseline and 1 h after carbidopa + 5-HTP show distinct oxidation peaks (~0.1 V for DA, ~0.28 V for 5-HT). (B) In vivo SWV detection of 5-HT in the mouse striatum. Following carbidopa and 5-HTP (i.p.) administration, SWV peak amplitude progressively increases over time. A corresponding positive shift in peak potential is observed with rising 5-HT levels. (C) Representative raw broadband continuous extracellular trace recorded from an MEA channel. (D) Overlaid spike waveforms extracted from the same channel, demonstrating consistency in waveform shape across detected events.

recording quality, in agreement with their low-impedance and high-surface-area properties.

Together, these data demonstrate that MXene/PEDOT coatings enable dual-mode neurochemical and electrophysiological functionality on Pt-MEA microelectrodes in vivo. It is important to note that SWV and electrophysiological measurements were performed separately in this study to avoid SWV-induced artifacts and to independently validate performance in each modality. This approach ensures that the observed improvements in both neurochemical sensing and electrophysiological signal quality arise from the MXene/PEDOT coating itself.

In future implementations, dual-mode operation could be achieved either through rapid sequential switching between acquisition modes on the same electrodes or by using spatially distinct recording and sensing sites within the same MEA, combined with post-processing strategies to mitigate SWV-related artifacts [31]. Since SWV is designed for tonic detection, rapid fluctuations in analyte concentration are not expected to be captured, and therefore the temporal offset introduced by sequential acquisition is not a major limitation for the intended measurements. These approaches would enable near-simultaneous correlation of neurochemical and electrophysiological signals while preserving data fidelity.

In future work, this dual capability could be leveraged to investigate how changes in monoamine signaling are coupled to local circuit activity during behavior, disease progression, and pharmacological interventions.

3 | Conclusion

In this work, we evaluated for the first time the in vivo performance of $Ti_3C_2T_x$ MXene/PEDOT composite coatings on flexible MEAs for tonic neurochemical multianalyte sensing. By integrating MXene/PEDOT onto both flexible GC-MEAs and metal-based Pt-MEAs, we established a versatile materials strategy that addresses longstanding challenges in tonic neurotransmitter detection while preserving high-quality neural signal acquisition.

16163028, 2026, 46, Downloaded from https://advanced.onlinelibrary.wiley.com/doi/10.1002/adfm.75402 by University Degli Studi Di Genova, Wiley Online Library on [28/06/2026]. See the Terms and Conditions (https://onlinelibrary.wiley.com/terms-and-conditions) on Wiley Online Library for rules of use; OA articles are governed by the applicable Creative Commons License

When applied to GC-MEAs, MXene/PEDOT enhanced charge transfer, reduced impedance, and improved resistance to electrochemical fouling and biofouling, enabling stable SWV detection of tonic DA and 5-HT, both individually and simultaneously, at physiologically relevant concentrations across multiple brain regions. The ability to resolve basal neurotransmitter levels in vivo, supported by pharmacological validation and sustained signal stability during prolonged scanning, demonstrates the suitability of this composite for monitoring slow neurotransmitter dynamics. In combination with the previously demonstrated GC-MEA compatibility with electrophysiology and FSCV-based phasic measurements, these results support a path toward a single multianalyte, multi-timescale platform capable of capturing tonic and phasic neurochemistry alongside electrical activity.

Importantly, extending this strategy to Pt-MEAs showed that MXene/PEDOT coating conferred neurotransmitter sensitivity to metal electrodes that are otherwise limited to electrophysiological recording, while improving signal quality compared to uncoated electrodes. MXene/PEDOT-coated Pt-MEAs preserved electrophysiological performance, including reliable single-unit spiking activity in vivo, while enabling SWV-based detection of DA and 5-HT. This dual capability provides a practical route for transforming conventional electrophysiology platforms into multimodal, multi-analyte neural interfaces.

Collectively, these findings suggest that MXene/PEDOT composites represent a promising electroactive material for in vivo neural interfaces, exhibiting strong resistance to electrochemical fouling and biofouling while supporting stable neurochemical sensing under acute, physiologically relevant conditions. Although this work focused on acute in vivo validation, the observed interfacial stability motivates future studies to evaluate chronic performance. By enabling multianalyte, multi-timescale neurochemical measurements concurrently with electrophysiological recording, MXene/PEDOT may serve as an important enabling material for the development of next-generation multimodal neural interfaces.

4 | Methods

4.1 | Glassy Carbon Microelectrode Array Fabrication

The fabrication of GC-MEAs was performed following the procedure described in our previous studies [32–34]. The fabricated probes contained 5–8 microelectrodes along a 100–140 μm-wide shank, with circular (50 μm diameter, ~1,963 μm^2) or oval (75 μm × 35 μm, ~2,062 μm^2) electroactive areas designed for electrochemical measurements.

Fabrication began with a 4-inch silicon wafer coated with a 1 μm-thick thermal SiO_2 layer (University Wafer Inc., Boston, MA, USA). The wafer was sequentially cleaned in acetone, isopropanol, and deionized (DI) water, dried using a nitrogen (N_2) spray gun, and placed on a hot plate at 150°C for 5 min. Surface activation was performed by O_2 plasma treatment in a reactive ion etcher (RIE, MICRO-RIE 800, Technics Inc., Anaheim, CA, USA) operated at 300 mTorr and 150 W for 60 s.

Following plasma activation, SU-8 3035 (Kayaku Advanced Materials, Westborough, MA, USA) was spin-coated at 3000 rpm for 1 min, soft-baked at 65°C for 5 min and 95°C for 5 min, and patterned using a custom-designed photomask and a MA/BA6 Mask/Bond Aligner (Süss MicroTec, Garching, Germany) with an exposure dose of 350 mJ cm^{-2}. After exposure, the wafer underwent post-exposure baking at 65°C for 1 min and 95°C for 3 min. Development was performed in SU-8 developer (Kayaku Advanced Materials) for 1 min, followed by rinsing with isopropanol and DI water. The patterned SU-8 was then hard-baked at 200°C and 150°C for 5 min each and cooled to below 65°C.

Pyrolysis of the negative SU-8 resist was carried out following previously reported procedures from our lab [32–34, 38, 97], in a high-temperature split tube furnace (STF 1200 Tube Furnace, Across International, Livingston, NJ, United States). The sample was heated to 900°C with a temperature ramp-up at a rate of 5°C min^{-1}, then maintained at 900°C under 15 standard cubic centimeters per minute (sccm) N_2 (Airgas, Radnor Township, PA, United States) at 0.8 Torr for 60 min. The sample was then slowly cooled to room temperature at 3°C/min. After pyrolysis, the wafer was cleaned again with acetone, isopropanol, and DI water, dried with N_2, and treated with O_2 plasma using RIE to enhance surface adhesion.

The cleaned wafer was then spin-coated with SU-8 5 (Kayaku Advanced Materials) at 3000 rpm for 1 min, soft-baked at 65°C for 3 min and 95°C for 5 min, and patterned with a UV exposure dose of 200 mJ cm^{-2} to define the bottom insulation layer and open vias connecting the GC electrodes to subsequent metal traces. Post-exposure baking was carried out at 65°C for 1 min and 95°C for 3 min. The wafer was developed in SU-8 developer, rinsed with isopropanol and DI water, and hard-baked as previously described.

Next, APOL-LO 3204 (KemLab, Woburn, MA, USA) was spin-coated at 3000 rpm for 1 min and baked at 110°C for 1 min. The photoresist was exposed with a UV dose of 145 mJ cm^{-2} to define a sacrificial mask for subsequent metal lift-off. Following a post-exposure bake at 110°C for 1 min, the wafer was developed using a TMAH-based developer (KemLab).

Metal deposition was performed by sputtering 15 nm of chromium, 85 nm of gold, and 20 nm of platinum sequentially. The lift-off process was carried out by immersing the wafer in acetone, followed by rinsing with isopropanol to remove residual debris. The wafer was then cleaned again with acetone, isopropanol, and DI water, dried with N_2, and spin-coated with SU-8 5 (Kayaku Advanced Materials) at 1000 rpm for 1 min.

A soft-bake was performed at 65°C for 5 min and 95°C for an additional 5 min. This SU-8 layer was exposed to a UV dose of 200 mJ cm^{-2} to define the top insulation layer, followed by post-exposure baking at 65°C for 2 min and 95°C for 3 min. Development was carried out in SU-8 developer, and the wafer was rinsed with isopropanol and DI water, then hard-baked to complete insulation.

Finally, the MEAs were released from the wafer by immersion in a 1:7 buffered oxide etchant inside an acid hood for 4–6 h.

16163028, 2026, 46, Downloaded from https://advanced.onlinelibrary.wiley.com/doi/10.1002/adfm.75402 by University Degli Studi Di Genova, Wiley Online Library on [28/06/2026]. See the Terms and Conditions (https://onlinelibrary.wiley.com/terms-and-conditions) on Wiley Online Library for rules of use; OA articles are governed by the applicable Creative Commons License

4.2 | Platinum Microelectrode Array Fabrication

Fabrication began with a 4-inch silicon wafer coated with a 1 μm-thick thermal SiO_2 layer (University Wafer Inc., Boston, MA, USA). The wafer was sequentially rinsed with acetone, isopropanol, and deionized (DI) water, then dried using a nitrogen (N_2) spray gun. It was further dried on a hot plate at 150°C for 5 min. Surface activation was performed using O_2 plasma in a reactive ion etcher (RIE, MICRO-RIE 800, Technics Inc., Anaheim, CA, USA) operated at 300 mTorr and 150 W for 60 s.

Following plasma treatment, SU-8 5 (Kayaku Advanced Materials, Westborough, MA, USA) was spin-coated at 3000 rpm for 1 min. The coated wafer was soft-baked at 65°C for 5 min and 95°C for an additional 5 min. Photolithographic patterning was performed using a custom-designed photomask and a MA/BA6 Mask/Bond Aligner (Süss MicroTec, Garching, Germany). This first SU-8 layer was exposed to UV light with a dose of 200 mJ cm^{-2} to define the bottom insulation layer, followed by a post-exposure bake at 65°C for 1 min and 95°C for 3 min. The wafer was developed using SU-8 developer (Kayaku Advanced Materials), rinsed with isopropanol and DI water, and hard-baked as described above.

Next, an APOL-LO 3204 layer (KemLab, Woburn, MA, USA) was spin-coated at 3000 rpm for 1 min and baked at 110°C for 1 min. The layer was exposed with a UV dose of 145 mJ cm^{-2} to define a sacrificial mask for subsequent metal lift-off. After a post-exposure bake at 110°C for 1 min, the wafer was developed using a TMAH-based developer (KemLab).

Metal deposition was performed by sputtering sequential layers of chromium (15 nm), gold (85 nm), and platinum (20 nm). The lift-off process was carried out by immersing the wafer in acetone, followed by rinsing with isopropanol to remove residual debris. The wafer was then cleaned again with acetone, isopropanol, and DI water, dried with an N_2 spray gun, and spin-coated with SU-8 5 (Kayaku Advanced Materials) at 3000 rpm for 1 min.

A soft-bake was conducted at 65°C for 5 min and 95°C for another 5 min. This SU-8 layer was exposed with a UV dose of 200 mJ cm^{-2} to define the top insulation layer and to open the electrode and pad sites, followed by a post-exposure bake at 65°C for 2 min and 95°C for 3 min. Development was performed using SU-8 developer, and the wafer was rinsed with isopropanol and DI water, then hard-baked to finalize the insulation.

Finally, the microelectrode arrays (MEAs) were released from the wafer by immersion in a 1:7 buffered oxide etchant within an acid hood for 4–6 h.

4.3 | MXene Preparation

4.3.1 | Synthesis of Ti_3AlC_2 MAX Phase and $Ti_3C_2T_x$ MXene

Elemental titanium (Ti, -325 mesh, 99%, Thermo Scientific), aluminum (Al, -325 mesh, 99.5%, Thermo Scientific), and graphite (C, 7–11 μm, 99%, Alfa Aesar) powders were combined in a molar ratio of 3.00 : 1.20 : 1.88. The mixture was homogenized in a high-density polyethylene (HDPE) bottle containing ten 10 mm yttria-stabilized zirconia (YSZ) balls using a Turbula T2F mixer at 56 rpm for 3 h. The blended powder was transferred to an alumina crucible and placed in the center of a tube furnace under a constant argon flow (0.2 L min^{-1}). The temperature was increased to 1600°C at 5°C min^{-1} and maintained for 2 h, followed by natural cooling to room temperature. The resulting sintered Ti_3AlC_2 block was ground and sieved to obtain powders with particle sizes below 45 μm.

The $Ti_3C_2T_x$ MXene was produced by selective removal of aluminum layers from Ti_3AlC_2 using a mixed fluoride–acid etchant. For each gram of Ti_3AlC_2, 20 mL of 9 M hydrochloric acid (HCl, Fisher Chemical) containing potassium fluoride (KF, 99%, Thermo Scientific) was prepared such that the molar ratio of KF to Ti_3AlC_2 was 9:1. The precursor powder was added slowly to the etchant while stirring at 400 rpm and kept at 45°C for 72 h. The obtained slurry was divided into 50 mL centrifuge tubes (one per 0.5 g of precursor) and repeatedly washed with deionized water by centrifugation (3500 rpm, 2 min) and redispersion until the pH of the supernatant exceeded 6, yielding multilayer $Ti_3C_2T_x$.

4.3.2 | Delamination and Aerogel Formation of $Ti_3C_2T_x$ MXene

For delamination, 1 g of the washed $Ti_3C_2T_x$ powder was dispersed in 20 mL of 1 M tetramethylammonium hydroxide (TMAH, Thermo Scientific) and stirred at ambient temperature for 24 h. The dispersion was centrifuged at 3500 rpm for 5 min and washed twice with deionized water to remove residual salts. The resulting sediment was ultrasonicated for 1 h and centrifuged again at 3500 rpm for 30 min to separate the delaminated nanosheets. The supernatant containing single- or few-layer $Ti_3C_2T_x$ nanosheets was frozen in liquid nitrogen and freeze-dried at −50°C under vacuum for 72 h, yielding the $Ti_3C_2T_x$ aerogel.

4.4 | Morphological Characterization

Optical characterization was performed using high-resolution imaging with a VK-X150 3D scanning confocal microscope (Keyence America, Itasca, IL, USA). Scanning electron microscopy (SEM) and elemental analysis of the GC MEAs surfaces were conducted using a HITACHI S-4800 field-emission scanning electron microscope equipped with a Bruker XFlash 6160 energy-dispersive spectroscopy (EDS) system (Hitachi Global, Irvine, CA, USA). EDS was employed to identify and quantify the elemental composition on the electrode surfaces.

4.5 | MXene/PEDOT Coating and Electrochemical Characterization

An aqueous solution was prepared by mixing 2 mL of deionized water, 16 mg of $Ti_3C_2T_x$ aerogel, and 1 mg of poly(sodium 4-styrenesulfonate) (PSS, Sigma–Aldrich, St. Louis, MO, USA). The mixture was sonicated using a probe sonicator (2 s on, 2 s off, 20% power, 1.6 mm tip, Q500 Sonicator, QSonica LLC, Newtown, CT, USA). Subsequently, 5 μL of polyethylene glycol (PEG 400) was added to enhance the stability of the dispersion and prevent

16163028, 2026, 46, Downloaded from https://advanced.onlinelibrary.wiley.com/doi/10.1002/adfm.75402 by University Degli Studi Di Genova, Wiley Online Library on [28/06/2026]. See the Terms and Conditions (https://onlinelibrary.wiley.com/terms-and-conditions) on Wiley Online Library for rules of use; OA articles are governed by the applicable Creative Commons License

precipitation. The solution was then sonicated for an additional 30 min. Following this, 20 μL of 3,4-ethylenedioxythiophene (EDOT; Sigma–Aldrich, St. Louis, MO, USA) was added, and the final sonication step was carried out for 10 min. For the electropolymerization, the electrodes were immersed in the prepared solution using a three-electrode electrochemical cell configuration consisting of a platinum counter electrode, an Ag/AgCl wire reference electrode, and the working electrode. Chronoamperometry was performed at a constant potential of 0.9 V. The electrodeposition was terminated upon reaching a total charge density of 75 mC cm^{-2}. This charge density yielded the best trade-off between sensitivity and impedance. As a control, PEDOT:poly(sodium 4-styrenesulfonate) (PEDOT:PSS) was electrodeposited from an aqueous solution containing the same EDOT concentration and 0.8 wt.% PSS (Sigma–Aldrich, USA), using the same electropolymerization conditions.

Electrochemical impedance spectroscopy was employed to characterize the electrode–electrolyte interface before and after deposition of the MXene/PEDOT coating. Measurements were performed by applying a 10 mV (RMS) sinusoidal perturbation superimposed on the open-circuit potential, with the frequency swept from 1 Hz to 10 kHz.

Cyclic voltammetry was conducted to evaluate the capacitive behavior of the GC-MEAs before and after coating. The potential was swept between 0.8 and −0.6 V vs. Ag/AgCl at a scan rate of 100 mV s^{-1}. The charge storage capacity (CSC, in mC cm^{-2}) was calculated from the integrated area under the CV curve, according to:

$CSC = \int i \, dt / A$ over an entire CV cycle, where i is the current, t is time, and A is the geometric surface area of the electrode.

All in vitro EIS and CV measurements were conducted in 1× phosphate-buffered saline (PBS; Sigma–Aldrich, St. Louis, MO, USA) using a three-electrode electrochemical cell with a platinum counter electrode and an Ag/AgCl wire reference electrode. Both the electropolymerization and electrochemical characterizations were carried out using a potentiostat/galvanostat (Autolab, Metrohm, Riverview, FL, USA).

4.6 | In Vitro Square Wave Voltammetry Detection

Building upon our previous work [32, 33, 40, 126], we optimized the square wave voltammetry parameters to enable simultaneous electrochemical detection of dopamine and serotonin using a MXene/PEDOT-coated electrode. The SWV measurements were performed with a potentiostat/galvanostat (Autolab, Metrohm, Riverview, FL, United States) configured in a three-electrode setup, comprising a platinum counter electrode and an Ag/AgCl reference electrode. The SWV waveform was applied repeatedly over a potential range of −0.2–0.45 V, with a step frequency of 40 Hz, a pulse amplitude of 50 mV, and a step height of 5 mV. Scans were acquired every 15 s, with the potential held at 0 V between measurements.

In vitro calibration of DA was carried out using freshly prepared DA solutions diluted in 1× PBS across concentrations ranging from 50 nM to 1 μM. Electrode sensitivity was determined from the slope of the linear portion of the calibration curve, relating the peak current at 0.15 V to DA concentration. The same calibration procedure was used for 5-HT, with the peak current at 0.28 V corresponding to 5-HT concentration.

4.7 | Stability and Fouling Tests

Electrochemical fouling and coating stability tests were performed using the optimized square-wave voltammetry waveform, which was continuously scanned in PBS solutions containing 1 μM DA or 1 μM 5-HT, respectively.

Sensing performance was continuously monitored using SWV, and coating stability was periodically evaluated using EIS. EIS measurements were recorded every hour for the first 8 h and approximately every 6 h thereafter to evaluate changes in charge transfer resistance and overall electrode functionality during continuous scanning.

Biofouling tests were conducted by immersing the electrodes in PBS containing 4 mg mL^{-1} bovine serum albumin (BSA), incubated at 37°C. SWV responses to 1 μM DA or 5-HT and EIS measurements were recorded after 1, 3, 5, and 10 h to evaluate sensitivity and coating stability.

Microelectrode selectivity was assessed by scanning the SWV waveform in PBS containing 1 μM DA, 1 μM 5-HT, 3 μM epinephrine (EPI), 30 μ uric acid (UA), or 500 μ ascorbic acid (AA), all obtained from Sigma Life Science (St. Louis, MO, USA). A single analyte was introduced at a time.

4.8 | In Vivo Experiments

Five male and four female mice (C57BL/6J, 8–12 weeks, 30–35 g; Jackson Laboratory, Bar Harbor, ME, United States) and two rats (Sprague–Dawley Wild type, Charles Rivers, Massachusetts USA) were used for the in vivo experiments. All animal care and procedures were performed under approval of the Louisiana Tech University Institutional Animal Care and Use Committee and in accordance with regulations specified by the Division of Laboratory Animal Resources. Mice were induced with 1.5%–1.8% isoflurane mixed with oxygen flow at 1 L min^{-1}, then maintained at 0.85%–1.25%. Rats were induced with 2% isoflurane mixed with oxygen flow at 1 L min^{-1}, then maintained at 1%–1.5%. Body temperature was maintained at 37°C with a thermostatically controlled heating pad (Harvard Apparatus, Holliston, MA, United States).

4.8.1 | In Vivo SWV Voltammetry of DA and 5-HT

The anesthetized mice were positioned on a heating pad (Harvard Apparatus, Holliston, MA, United States) to maintain the body temperature at 37°C, and their heads were stabilized using a stereotaxic frame (Narishige International United States, Inc. Amityville, United States). Then, the scalp and connective tissue covering the skull were carefully removed.

16163028, 2026, 46, Downloaded from https://advanced.onlinelibrary.wiley.com/doi/10.1002/adfm.75402 by University Degli Studi Di Genova, Wiley Online Library on [28/06/2026]. See the Terms and Conditions (https://onlinelibrary.wiley.com/terms-and-conditions) on Wiley Online Library for rules of use; OA articles are governed by the applicable Creative Commons License

For DA detection, a small craniotomy was performed over the dorsal striatum (DS; coordinates: 1 mm anterior to bregma, 1.5 mm lateral from the midline) using a high-speed dental drill (0.007 drill bit, Fine Science Tools, Inc., Foster City, CA, United States). Bone fragments were gently cleared using forceps while saline irrigation was applied to prevent heat accumulation during drilling. The MXene/PEDOT coated GC MEA was then lowered 3.5–4 mm beneath the cortical surface into the DS with the aid of a micromanipulator. Two additional small craniotomies were made: one contralaterally to place an Ag/AgCl reference electrode and another caudally for the placement of a bone screw serving as the counter electrode. EIS was recorded immediately after MEA implantation to confirm proper electrode function. Subsequently, the tonic DA response was measured by applying the SWV waveform continuously over a 20 min period. After registering the basal level of dopamine, mice were administered with 2 mg kg^{-1} intraperitoneal (i.p.) raclopride, a selective antagonist on D2 dopamine receptors (Sigma–Aldrich, St. Louis, MO, United States), and 20 mg kg^{-1} i.p. nomifensine, a dopamine reuptake inhibitor (Sigma–Aldrich, St. Louis, MO, United States) [33]. After the injection the response was measured for 1 h. For 5-HT measurements, the mouse underwent the same surgical procedure described above but in different areas: prefrontal cortex (AP 1.7, ML 0.3, DV 1.5), striatum (AP 1, ML 1.5, DV 4) and amygdala (AP 3, ML -1.8, DV 4.5). Following the recording of basal 5-HT levels, carbidopa (Thermo Fisher Scientific, Waltham, MA, USA) was administered intraperitoneally (i.p.) at a dose of 25 mg kg^{-1} to inhibit peripheral aromatic L-amino acid decarboxylase activity. 20 min later, 5-hydroxytryptophan (5-HTP), (Thermo Fisher Scientific, Waltham, MA, USA) a serotonin precursor, was injected i.p. at a dose of 200 mg kg^{-1} [103]. Both compounds were dissolved in pre-warmed saline prior to injection.

SWV and EIS measurements were performed using a potentiostat/galvanostat (Autolab, Metrohm, Riverview, FL, United States) connected to a three-electrode setup comprising the working electrode, a bone screw as the counter electrode, and an Ag/AgCl wire as the reference electrode. DA peaks were extracted from the non-faradaic background current of each SWV scan by subtracting a polynomial baseline, following the method previously described by [40]. DA concentrations in all in vivo experiments were quantified by converting the SWV peak currents into concentration values using the pre-calibrated electrode sensitivity, as outlined in previous studies [32, 33, 40]. At the end of the experiments, the MXene/PEDOT coated electrodes were carefully explanted, and the animals were euthanized following institutional guidelines and approved protocols.

4.8.2 | Electrophysiological Recording

4.8.2.1 | Saline and in Vivo recording, filtering, and spike sorting. To reduce the number of animals required, we first performed controlled experiments in saline. The MEA probes were also evaluated in a saline bath to assess signal fidelity under controlled conditions. Electrodes were immersed in a beaker filled with saline (0.9% Sodium Chloride). The saline bath was connected to the audio output of a PC using an audio jack-to-RCA adapter cable, with the leads positioned at opposite ends of the beaker. Pre-recorded simulated spike signals were played through the audio output, generating electrical activity within the saline medium. These signals were then detected by the MEA probes and recorded using the data acquisition system. This setup enabled assessment of signal quality, including signal-to-noise characteristics.

Mice and rats were anesthetized and secured as described in Section 4.8.1. The stereotactic arm holding the MEAs was mounted onto a KOPF stereotactic frame. The somatosensory (ML 3 mm, AP –1.3 mm, DV 1.1 mm, mouse; ML 4.2 mm, AP -2.0 mm, DV 2.5 mm, rat) and motor cortices (ML 3 mm, AP +1.5 mm, DV 1 mm, mouse; ML 1.9 mm, AP 0.0 mm, DV 2 mm, rat), were specifically targeted for acute recordings. Each MEA was connected to a 16-channel Omnetics connector, which interfaced with the Kontex X-Headstage. The headstage was connected to the Kontex ONE data acquisition (DAQ) system via a μ-HDMI–to–HDMI cable for recording neuronal activities from the MEA.

Neuronal activity was recorded and visualized in real time with the Allego software, part of the Radiens analytical suite (Neuronexus). Signals were sampled at 32 kHz and exported in *xdat* format for subsequent processing in MATLAB (MathWorks, Natick, MA).

Offline filtering and spike sorting were performed using a custom MATLAB interface (R2023a) developed in the Kumbhare Lab. Spikes were detected using manually defined thresholds, and waveform features (first three components of PCA) were projected into a 3D feature space. Single units were then isolated using a hybrid approach combining automated valley-seeking and manual sorting techniques, including k-means clustering, contour separation, and waveform-crossing methods. Sorted clusters were visually inspected to exclude artifacts and verify signal integrity. The timestamps of the final spike trains were saved for downstream analyses.

4.8.2.2 | Preprocessing. Broadband neural data were acquired without hardware filtering and subsequently processed offline according to the analysis type. For spike (single-unit) analyses, signals were band-pass filtered between 300 and 5000 Hz. Notch filters were applied to remove power line noise at 60 Hz and its harmonics.

4.8.2.3 | Signal to noise ratio calculations (SNR). For each isolated unit, a representative waveform was obtained by computing the median across all detected spike waveforms. Spike amplitude was quantified as the peak-to-peak voltage (Vpp) of this median waveform.

4.8.2.4 | Baseline noise. Baseline noise was estimated from the filtered trace using a robust estimator of standard deviation:

$$\sigma_n = \frac{\text{median}(\,|x - \text{median}\,(x)|}{0.6745} \quad (1)$$

where x is the band-pass filtered signal.

The signal-to-noise ratio (SNR) was computed as:

$$\text{SNR} = \frac{V_{pp}}{2\sigma_n} \quad (2)$$

16163028, 2026, 46, Downloaded from https://advanced.onlinelibrary.wiley.com/doi/10.1002/adfm.75402 by University Degli Studi Di Genova, Wiley Online Library on [28/06/2026]. See the Terms and Conditions (https://onlinelibrary.wiley.com/terms-and-conditions) on Wiley Online Library for rules of use; OA articles are governed by the applicable Creative Commons License

Acknowledgements

The authors would like to thank Ashok Sigdel, Davis Bailey, Dr. Arden Moore and all the staff of the Institute of Micromanufacturing (IfM) at Louisiana Tech University for their technical support and the use of the facilities. MXene synthesis and characterization at Tulane University were supported by the National Science Foundation under Grant No. DMR-2048164. MEA fabrication, characterization, and in vitro and in vivo validation at Louisiana Tech University were supported by the National Institutes of Health (R01NS126454 and R21MH128803) and the National Science Foundation (CAREER-2443918). Electrophysiological measurements were supported by a New Investigator Grant from the Heffter Research Institute to Dr. Deepak Kumbhare.

Funding

NIH RO1NS126454; NIH R21MH128803; NSF CAREER-2443918; NSF DMR-2048164; New Investigator Heffter Research Institute Grant to Dr. Deepak Kumbhare.

Conflicts of Interest

The authors declare no conflicts of interest.

Data Availability Statement

The data that support the findings of this study are available from the corresponding author upon reasonable request.

References

1. Y. Park, T. S. Chung, G. Lee, and J. A. Rogers, "Materials Chemistry of Neural Interface Technologies and Recent Advances in Three-Dimensional Systems," *Chemical Reviews* 122, no. 5 (2021): 5277–5316, https://doi.org/10.1021/acs.chemrev.1c00639.

2. A. A. Ahmed, N. Alegret, B. Almeida, et al., "Interfacing with the Brain: How Nanotechnology Can Contribute," *ACS nano* 19, no. 11 (2025): 10630–10717, https://doi.org/10.1021/acsnano.4c10525.

3. H.-Y. Lu, E. S. Lorenc, H. Zhu, et al., "Multiscale Neural Decoding and Analysis," *Journal of Neural Engineering* 18, no. 4 (2021): 045013, https://doi.org/10.1088/1741-2552/ac160f.

4. N. K. Popova and V. S. Naumenko, "Neuronal and Behavioral Plasticity: The Role of Serotonin and BDNF Systems Tandem," *Expert Opinion on Therapeutic Targets* 23, no. 3 (2019): 227–239, https://doi.org/10.1080/14728222.2019.1572747.

5. E. Bustos, J. Manríquez, A. L. Colín-González, E. Rangel-López, and A. Santamaría, "Electrochemical Detection of Neurotransmitters in the Brain and Other Molecules with Biological Activity in the Nervous System: Dopamine Analysis," *Current Organic Chemistry* 24, no. 21 (2020): 2498–2507, https://doi.org/10.2174/1385272824666200204121746.

6. K. A. Jennings, "A Comparison of the Subsecond Dynamics of Neurotransmission of Dopamine and Serotonin," *ACS Chemical Neuroscience* 4, no. 5 (2013): 704–714, https://doi.org/10.1021/cn4000605.

7. I. Gonzalez-Burgos and A. Feria-Velasco, "Serotonin/Dopamine Interaction in Memory Formation," *Progress in Brain Research* 172 (2008): 603–623.

8. G. Di Giovanni, E. Esposito, and V. Di Matteo, "Role of Serotonin in Central Dopamine Dysfunction," *CNS Neuroscience & Therapeutics* 16, no. 3 (2010): 179–194, https://doi.org/10.1111/j.1755-5949.2010.00135.x.

9. H. H. Jung, J. Ha, J. Park, et al., "Highly Deformable Double-Sided Neural Probe with All-in-One Electrode System for Real-Time in Vivo Detection of Dopamine for Parkinson's Disease," *Advanced Functional Materials* 34, no. 4 (2024): 2311436, https://doi.org/10.1002/adfm.202311436.

10. M. E. J. Obien, K. Deligkaris, T. Bullmann, D. J. Bakkum, and U. Frey, "Revealing Neuronal Function through Microelectrode Array Recordings," *Frontiers in Neuroscience* 8 (2015): 423, https://doi.org/10.3389/fnins.2014.00423.

11. C. T. Nordhausen, P. J. Rousche, and R. A. Normann, "Optimizing Recording Capabilities of the Utah Intracortical Electrode Array," *Brain Research* 637, no. 1-2 (1994): 27–36, https://doi.org/10.1016/0006-8993(94)91213-0.

12. R. A. Normann and E. Fernandez, "Clinical Applications of Penetrating Neural Interfaces and Utah Electrode Array Technologies," *Journal of Neural Engineering* 13, no. 6 (2016): 061003, https://doi.org/10.1088/1741-2560/13/6/061003.

13. N. A. Blum, B. G. Carkhuff, H. K. Charles, R. L. Edwards, and R. A. Meyer, "Multisite Microprobes for Neural Recordings," *IEEE Transactions on Biomedical Engineering* 38, no. 1 (1991): 68–74, https://doi.org/10.1109/10.68211.

14. M. D. Johnson, R. K. Franklin, M. D. Gibson, R. B. Brown, and D. R. Kipke, "Implantable Microelectrode Arrays for Simultaneous Electrophysiological and Neurochemical Recordings," *Journal of Neuroscience Methods* 174, no. 1 (2008): 62–70, https://doi.org/10.1016/j.jneumeth.2008.06.036.

15. D. J. Edell, V. V. Toi, V. M. McNeil, and L. Clark, "Factors Influencing the Biocompatibility of Insertable Silicon Microshafts in Cerebral Cortex," *IEEE Transactions on Biomedical Engineering* 39, no. 6 (1992): 635–643, https://doi.org/10.1109/10.141202.

16. D. Szarowski, M. Andersen, S. Retterer, et al., "Brain Responses to Micro-Machined Silicon Devices," *Brain research* 983, no. 1-2 (2003): 23–35, https://doi.org/10.1016/S0006-8993(03)03023-3.

17. T. D. Kozai, A. S. Jaquins-Gerstl, A. L. Vazquez, A. C. Michael, and X. T. Cui, "Brain Tissue Responses to Neural Implants Impact Signal Sensitivity and Intervention Strategies," *ACS Chemical Neuroscience* 6, no. 1 (2015): 48–67, https://doi.org/10.1021/cn500256e.

18. S. M. Wellman, J. R. Eles, K. A. Ludwig, et al., "A Materials Roadmap to Functional Neural Interface Design," *Advanced Functional Materials* 28, no. 12 (2018): 1701269.

19. J. Shi and Y. Fang, "Flexible and Implantable Microelectrodes for Chronically Stable Neural Interfaces," *Advanced Materials* 31, no. 45 (2019): 1804895.

20. R. C. Engstrom, R. M. Wightman, and E. W. Kristensen, "Diffusional Distortion in the Monitoring of Dynamic Events," *Analytical Chemistry* 60, no. 7 (1988): 652–656, https://doi.org/10.1021/ac00158a010.

21. K. Kawagoe, P. Garris, D. Wiedemann, and R. Wightman, "Regulation of Transient Dopamine Concentration Gradients in the Microenvironment Surrounding Nerve Terminals in the Rat Striatum," *Neuroscience* 51, no. 1 (1992): 55–64, https://doi.org/10.1016/0306-4522(92)90470-M.

22. H. N. Schwerdt, M. Kim, and E. Karasan, "Subcellular Electrode Arrays for Multisite Recording of Dopamine in Vivo," in *2017 IEEE 30th International Conference on Micro Electro Mechanical Systems (MEMS)* (IEEE, 2017), 549–552, https://doi.org/10.1109/MEMSYS.2017.7863465.

23. J. Agorelius, F. Tsanakalis, A. Friberg, P. T. Thorbergsson, L. M. E. Pettersson, and J. Schouenborg, "An Array of Highly Flexible Electrodes with a Tailored Configuration Locked by Gelatin during Implantation—Initial Evaluation in Cortex Cerebri of Awake Rats," *Frontiers in neuroscience* 9 (2015): 331, https://doi.org/10.3389/fnins.2015.00331.

24. E. Castagnola, L. Maiolo, and E. Maggiolini, "Ultra-flexible and Brain-conformable Micro-electrocorticography Device with Low Impedance PEDOT-Carbon Nanotube Coated Microelectrodes," in *2013 6th International IEEE/EMBS Conference on Neural Engineering (NER)* (IEEE, 2013), 927–930.

25. S. Nimbalkar, E. Castagnola, A. Balasubramani, et al., "Ultra-capacitive Carbon Neural Probe Allows Simultaneous Long-term Electrical Stimulations and High-resolution Neurotransmitter Detection," *Scientific reports* 8, no. 1 (2018): 1–14, https://doi.org/10.1038/s41598-41018-25198-x.

16163028, 2026, 46, Downloaded from https://advanced.onlinelibrary.wiley.com/doi/10.1002/adfm.75402 by University Degli Studi Di Genova, Wiley Online Library on [28/06/2026]. See the Terms and Conditions (https://onlinelibrary.wiley.com/terms-and-conditions) on Wiley Online Library for rules of use; OA articles are governed by the applicable Creative Commons License

26. J. Jeong, G. Heo, Y. W. Kwon, et al., "Biomimetic Design of Biocompatible Neural Probes for Deep Brain Signal Monitoring and Stimulation: Super Static Interface for Immune Response-Enhanced Contact," *Advanced Functional Materials* 35 (2025): 2417727, https://doi.org/10.1002/adfm.202417727.

27. M. Y. Pwint, D. Shi, and X. T. Cui, "Buckling-Resistant and Trace-Stacked (BRATS) Design Enables Aid-Free Implantation of Flexible Multielectrode Array with Minimized Inflammatory Tissue Response," *Advanced Functional Materials* 36 (2025): 12565.

28. X. Liu, Y. Lu, and D. Kuzum, "High-density Porous Graphene Arrays Enable Detection and Analysis of Propagating Cortical Waves and Spirals," *Scientific Reports* 8, no. 1 (2018): 1–10, https://doi.org/10.1038/s41598-018-35613-y.

29. Y. Ou, A. M. Buchanan, C. E. Witt, and P. Hashemi, "Frontiers in Electrochemical Sensors for Neurotransmitter Detection: towards Measuring Neurotransmitters as Chemical Diagnostics for Brain Disorders," *Analytical Methods* 11, no. 21 (2019): 2738–2755, https://doi.org/10.1039/C9AY00055K.

30. Q. Cao, D. K. Hensley, N. V. Lavrik, and B. J. Venton, "Carbon Nanospikes Have Better Electrochemical Properties than Carbon Nanotubes due to Greater Surface Roughness and Defect Sites," *Carbon* 155 (2019): 250–257, https://doi.org/10.1016/j.carbon.2019.08.064.

31. U. Siwakoti, S. A. Jones, D. Kumbhare, X. T. Cui, and E. Castagnola, "Recent Progress in Flexible Microelectrode Arrays for Combined Electrophysiological and Electrochemical Sensing," *Biosensors* 15, no. 2 (2025): 100, https://doi.org/10.3390/bios15020100.

32. E. Castagnola, E. M. Robbins, D. D. Krahe, et al., "Stable in-vivo Electrochemical Sensing of Tonic Serotonin Levels Using PEDOT/CNT-coated Glassy Carbon Flexible Microelectrode Arrays," *Biosensors and Bioelectronics* 230 (2023): 115242, https://doi.org/10.1016/j.bios.2023.115242.

33. E. Castagnola, E. M. Robbins, B. Wu, et al., "Flexible Glassy Carbon Multielectrode Array for in Vivo Multisite Detection of Tonic and Phasic Dopamine Concentrations," *Biosensors* 12, no. 7 (2022): 540, https://doi.org/10.3390/bios12070540.

34. S. C. Sellen, U. Siwakoti, A. Sigdel, S. Zivanovic, and E. Castagnola, "Advancing Glassy Carbon Microelectrode Arrays for Neurochemical Sensing: Impact of Double Pyrolysis on Structure and Function," *Frontiers in Bioengineering and Biotechnology* 13 (2025): 1642063, https://doi.org/10.3389/fbioe.2025.1642063.

35. J. Li, Y. Liu, L. Yuan, et al., "A Tissue-Like Neurotransmitter Sensor for the Brain and Gut," *Nature* 606, no. 7912 (2022): 94–101, https://doi.org/10.1038/s41586-022-04615-2.

36. Y. Qi, D. Jang, J. Ryu, et al., "Stabilized Carbon Coating on Microelectrodes for Scalable and Interoperable Neurotransmitter Sensing," *Nature Communications* 16, no. 1 (2025): 3300, https://doi.org/10.1038/s41467-025-58388-z.

37. B. Fan, C. A. Rusinek, C. H. Thompson, et al., "Flexible, Diamond-based Microelectrodes Fabricated Using the Diamond Growth Side for Neural Sensing," *Microsystems & nanoengineering* 6, no. 1 (2020): 42.

38. E. Castagnola, S. Thongpang, M. Hirabayashi, et al., "Glassy Carbon Microelectrode Arrays Enable Voltage-Peak Separated Simultaneous Detection of Dopamine and Serotonin Using Fast Scan Cyclic Voltammetry," *The Analyst* 146, no. 12 (2021): 3955–3970, https://doi.org/10.1039/D1AN00425E.

39. E. Castagnola, N. W. Vahidi, S. Nimbalkar, et al., "In Vivo Dopamine Detection and Single Unit Recordings Using Intracortical Glassy Carbon Microelectrode Arrays," *MRS advances* 3, no. 29 (2018): 1629–1634, https://doi.org/10.1557/adv.2018.98.

40. I. M. Taylor, N. A. Patel, N. C. Freedman, E. Castagnola, and X. T. Cui, "Direct in Vivo Electrochemical Detection of Resting Dopamine Using Poly (3, 4-ethylenedioxythiophene)/Carbon Nanotube Functionalized Microelectrodes," *Analytical chemistry* 91, no. 20 (2019): 12917–12927, https://doi.org/10.1021/acs.analchem.9b02904.

41. X. Wang, M. Xu, H. Yang, et al., "Ultraflexible Neural Electrodes Enabled Synchronized Long-term Dopamine Detection and Wideband Chronic Recording Deep in Brain," *ACS nano* 18, no. 50 (2024): 34272–34287, https://doi.org/10.1021/acsnano.4c12429.

42. E. He, S. Xu, Y. Dai, et al., "SWCNTs/PEDOT: PSS-modified Microelectrode Arrays for Dual-mode Detection of Electrophysiological Signals and Dopamine Concentration in the Striatum under Isoflurane Anesthesia," *ACS sensors* 6, no. 9 (2021): 3377–3386, https://doi.org/10.1021/acssensors.1c01241.

43. B. Wu, E. Castagnola, C. A. McClung, and X. T. Cui, "PEDOT/CNT Flexible MEAs Reveal New Insights into the Clock Gene's Role in Dopamine Dynamics," *Advanced Science* 11 (2024): 2308212.

44. H. Rafi and A. G. Zestos, "Review—Recent Advances in FSCV Detection of Neurochemicals via Waveform and Carbon Microelectrode Modification," *Journal of The Electrochemical Society* 168, no. 5 (2021): 057520, https://doi.org/10.1149/1945-7111/ac0064.

45. P. Puthongkham and B. J. Venton, "Recent Advances in Fast-scan Cyclic Voltammetry," *The Analyst* 145, no. 4 (2020): 1087–1102, https://doi.org/10.1039/C9AN01925A.

46. J. G. Roberts and L. A. Sombers, "Fast-Scan Cyclic Voltammetry: Chemical Sensing in the Brain and beyond," *Analytical Chemistry* 90, no. 1 (2018): 490–504, https://doi.org/10.1021/acs.analchem.7b04732.

47. M. Naguib, O. Mashtalir, J. Carle, et al., "Two-dimensional Transition Metal Carbides," *ACS Nano* 6, no. 2 (2012): 1322–1331, https://doi.org/10.1021/nn204153h.

48. B. Anasori, M. Naguib, and G. Editors, "Two-dimensional MXenes," *MRS Bulletin* 48, no. 3 (2023): 238–244, https://doi.org/10.1557/s43577-023-00500-z.

49. M. Downes, C. E. Shuck, B. McBride, J. Busa, and Y. Gogotsi, "Comprehensive Synthesis of $Ti_3C_2T_X$ from MAX Phase to MXene," *Nature Protocols* 19, no. 6 (2024): 1807–1834, https://doi.org/10.1038/s41596-024-00969-1.

50. C. Zhang and M. Naguib, *Transition Metal Carbides and Nitrides (MXenes) Handbook: Synthesis, Processing, Properties and Applications* (John Wiley & Sons, 2024), https://doi.org/10.1002/9781119869528.

51. M. A. Purbayanto, V. Presser, K. Skarżyński, M. Słoma, M. Naguib, and A. M. Jastrzębska, "MXenes: Multifunctional Materials for the Smart Cities of Tomorrow," *Advanced Functional Materials* 35, no. 10 (2025): 2409953, https://doi.org/10.1002/adfm.202409953.

52. K. Li, M. Liang, H. Wang, et al., "3D MXene Architectures for Efficient Energy Storage and Conversion," *Advanced Functional Materials* 30, no. 47 (2020): 2000842, https://doi.org/10.1002/adfm.202000842.

53. B. Xu and Y. Gogotsi, "MXenes: from Discovery to Applications," *Advanced Functional Materials* 30, no. 47 (2020): 2007011, https://doi.org/10.1002/adfm.202007011.

54. D. Nandi, S. Talande, A. Cheruvathoor Poulose, et al., "High Energy Density Asymmetric Aqueous Supercapacitor Based on a 2D Manganese Carbide as a Positive Electrode," *Advanced Functional Materials* (2025): e27953, https://doi.org/10.1002/adfm.202527953.

55. J. Yu, D. Qu, X. Wang, et al., "A Supercapacitor Driven by MXene Nanofluid Gel Electrolyte Induced the Synergistic High Ionic Migration Rate and Excellent Mechanical Properties," *Advanced Functional Materials* 35, no. 6 (2025): 2414934, https://doi.org/10.1002/adfm.202414934.

56. A. Iqbal, P. Sambyal, and C. M. Koo, "2D MXenes for Electromagnetic Shielding: a Review," *Advanced Functional Materials* 30, no. 47 (2020): 2000883, https://doi.org/10.1002/adfm.202000883.

57. H. Wang, Y. Jiang, Z. Ma, et al., "Hyperelastic, Robust, Fire-Safe Multifunctional MXene Aerogels with Unprecedented Electromagnetic Interference Shielding Efficiency," *Advanced Functional Materials* 33, no. 49 (2023): 2306884, https://doi.org/10.1002/adfm.202306884.

58. M. Wei, N. Wu, B. Li, et al., "From MXene to Multimodal-Responsive Smart, Durable Electromagnetic Interference Shielding

16163028, 2026, 46, Downloaded from https://advanced.onlinelibrary.wiley.com/doi/10.1002/adfm.75402 by University Degli Studi Di Genova, Wiley Online Library on [28/06/2026]. See the Terms and Conditions (https://onlinelibrary.wiley.com/terms-and-conditions) on Wiley Online Library for rules of use; OA articles are governed by the applicable Creative Commons License

Textiles," *Advanced Functional Materials* 35 (2025): 2424312, https://doi.org/10.1002/adfm.202424312.

59. C. Ma, M. G. Ma, C. Si, X. X. Ji, and P. Wan, "Flexible MXene-Based Composites for Wearable Devices," *Advanced Functional Materials* 31, no. 22 (2021): 2009524, https://doi.org/10.1002/adfm.202009524.

60. M. Li, Y. Zhang, L. Lian, et al., "Flexible Accelerated-Wound-Healing Antibacterial MXene-Based Epidermic Sensor for Intelligent Wearable Human-Machine Interaction," *Advanced Functional Materials* 32, no. 47 (2022): 2208141, https://doi.org/10.1002/adfm.202208141.

61. X. Zheng, S. Zhang, M. Zhou, et al., "MXene Functionalized, Highly Breathable and Sensitive Pressure Sensors with Multi-Layered Porous Structure," *Advanced Functional Materials* 33, no. 19 (2023): 2214880, https://doi.org/10.1002/adfm.202214880.

62. M. Sharifuzzaman, M. A. Zahed, M. S. Reza, et al., "MXene/Fluoropolymer-Derived Laser-Carbonaceous All-Fibrous Nanohybrid Patch for Soft Wearable Bioelectronics," *Advanced Functional Materials* 33, no. 21 (2023): 2208894, https://doi.org/10.1002/adfm.202208894.

63. B. Wang, Y. Sun, H. Ding, et al., "Bioelectronics-Related 2D Materials beyond Graphene: Fundamentals, Properties, and Applications," *Advanced Functional Materials* 30, no. 46 (2020): 2003732, https://doi.org/10.1002/adfm.202003732.

64. R. Garg, N. Driscoll, S. Shankar, et al., "Wearable High-Density MXene-Bioelectronics for Neuromuscular Diagnostics, Rehabilitation, and Assistive Technologies," *Small Methods* 7, no. 8 (2023): 2201318, https://doi.org/10.1002/smtd.202201318.

65. G. Li, B. C. Wyatt, F. Song, et al., "2D Titanium Carbide (MXene) Based Films: Expanding the Frontier of Functional Film Materials," *Advanced Functional Materials* 31, no. 46 (2021): 2105043, https://doi.org/10.1002/adfm.202105043.

66. V. Orts Mercadillo, K. C. Chan, M. Caironi, et al., "Electrically Conductive 2D Material Coatings for Flexible and Stretchable Electronics: a Comparative Review of Graphenes and MXenes," *Advanced Functional Materials* 32, no. 38 (2022): 2204772, https://doi.org/10.1002/adfm.202204772.

67. M. M. Hasan, M. M. Hossain, and H. K. Chowdhury, "Two-dimensional MXene-based Flexible Nanostructures for Functional Nanodevices: a Review," *Journal of Materials Chemistry A* 9, no. 6 (2021): 3231–3269, https://doi.org/10.1039/D0TA11103A.

68. S. Li, L. Ma, M. Zhou, et al., "New Opportunities for Emerging 2D Materials in Bioelectronics and Biosensors," *Current Opinion in Biomedical Engineering* 13 (2020): 32–41.

69. N. Driscoll, A. G. Richardson, K. Maleski, et al., "Two-Dimensional Ti_3C_2MXene for High-Resolution Neural Interfaces," *ACS nano* 12, no. 10 (2018): 10419–10429, https://doi.org/10.1021/acsnano.8b06014.

70. J. Li, F. Qi, C. Li, et al., "MXene-Enhanced Detachable Transistor Neuroprobe for Real-time Monitoring of Serotonin Dynamics in human Organoids and Living Brains," *Chemical Engineering Journal* 512 (2025): 162542, https://doi.org/10.1016/j.cej.2025.162542.

71. M. Yang, L. Wang, H. Lu, and Q. Dong, "Advances in MXene-based Electrochemical (bio) Sensors for Neurotransmitter Detection," *Micromachines* 14, no. 5 (2023): 1088, https://doi.org/10.3390/mi14051088.

72. A. M. Arjun, M. Shinde, and G. Slaughter, "Application of MXene in the Electrochemical Detection of Neurotransmitters: A Review," *IEEE Sensors Journal* 23, no. 15 (2023): 16456–16466, https://doi.org/10.1109/JSEN.2023.3285594.

73. A. Lipatov, M. Alhabeb, M. R. Lukatskaya, A. Boson, Y. Gogotsi, and A. Sinitskii, "Effect of Synthesis on Quality, Electronic Properties and Environmental Stability of Individual Monolayer Ti_3C_2MXene Flakes," *Advanced Electronic Materials* 2, no. 12 (2016): 1600255, https://doi.org/10.1002/aelm.201600255.

74. S. Gou, P. Li, S. Yang, G. Bi, and Z. Du, "High-Performance MXene/PEDOT-PSS Microscale Fiber Electrodes for Neural Recording and Stimulation," *Advanced Functional Materials* 35, no. 20 (2025): 2424236, https://doi.org/10.1002/adfm.202424236.

75. Q. Zeng, C. Xing, Z. Xu, et al., "Fast Electrodeposition of MXene/PDA Composites for High-Performance Bioelectronic Interfaces: an in Vitro Evaluation," *Advanced Functional Materials* 34, no. 23 (2024): 2312770, https://doi.org/10.1002/adfm.202312770.

76. F. Wang, F. Liang, Q. Chen, et al., "MXene-enhanced Hydrogel Cardiac Patch with High Electrical Conductivity, Mechanical Strength, and Excellent Biocompatibility," *Materials Today Electronics* 13 (2025): 100163, https://doi.org/10.1016/j.mtelec.2025.100163.

77. H. Vojoudi and M. B.-F. M. X. Soroush, "Synthesis and Versatile Applications," *Advanced Healthcare Materials* 14, no. 15 (2025): 2500359.

78. S. Kumar, S. M. Z. Mehdi, M. Taunk, et al., "Synergistic Effects of Polymer Integration on the Properties, Stability, and Applications of MXenes," *Journal of Materials Chemistry A* 13 (2025): 11050–11113, https://doi.org/10.1039/D4TA08094G.

79. J. Li, A. Levitt, N. Kurra, et al., "MXene-conducting Polymer Electrochromic Microsupercapacitors," *Energy Storage Materials* 20 (2019): 455–461, https://doi.org/10.1016/j.ensm.2019.04.028.

80. H. Riazi, S. K. Nemani, M. C. Grady, B. Anasori, and M. Soroush, "Ti_3C_2MXene–Polymer Nanocomposites and Their Applications," *Journal of Materials Chemistry A* 9, no. 13 (2021): 8051–8098, https://doi.org/10.1039/D0TA08023C.

81. K. A. S. Usman, S. Qin, L. C. Henderson, J. Zhang, D. Y. Hegh, and J. M. Razal, "$Ti_3C_2T_X$MXene: From Dispersions to Multifunctional Architectures for Diverse Applications," *Materials horizons* 8, no. 11 (2021): 2886–2912, https://doi.org/10.1039/D1MH00968K.

82. S. Wustoni, A. Saleh, J. K. El-Demellawi, et al., "MXene Improves the Stability and Electrochemical Performance of Electropolymerized PEDOT Films," *APL Materials* 8, no. 12 (2020): 121105, https://doi.org/10.1063/5.0023187.

83. A. E. Avila Ramirez, D. P. van der Laan, M. B. Shah, L. Wang, E. Zeglio, and A. Savva, "PEDOT:PSS—A Key Material for Bioelectronics," *Advanced Science* 13, no. 11 (2026): 13480, https://doi.org/10.1002/advs.202513480.

84. D. D. Zhou, X. T. Cui, A. Hines, and R. J. Greenberg, "Conducting Polymers in Neural Stimulation Applications," in *Implantable Neural Prostheses 2: Techniques and Engineering Approaches* (Springer, 2009), 217–252.

85. X. T. Cui and D. D. Zhou, "Poly (3, 4-ethylenedioxythiophene) for Chronic Neural Stimulation," *IEEE Transactions on Neural Systems and Rehabilitation Engineering* 15, no. 4 (2007): 502–508, https://doi.org/10.1109/TNSRE.2007.909811.

86. M. Z. Wrona and G. Dryhurst, "Electrochemical Oxidation of 5-hydroxytryptamine in Aqueous Solution at Physiological pH," *Bioorganic Chemistry* 18, no. 3 (1990): 291–317, https://doi.org/10.1016/0045-2068(90)90005-P.

87. A. M. Amani, L. Tayebi, E. Vafa, et al., "MXenes in Biosensing: Enhancing Sensitivity and Flexibility—A Review of Properties, Applications, and Future Directions, and Future Directions," *Sensing and Bio-Sensing Research* 47 (2025): 100732, https://doi.org/10.1016/j.sbsr.2024.100732.

88. D. Lu, H. Zhao, X. Zhang, Y. Chen, and L. Feng, "New Horizons for MXenes in Biosensing Applications," *Biosensors* 12, no. 10 (2022): 820, https://doi.org/10.3390/bios12100820.

89. U. Amara, I. Hussain, M. Ahmad, K. Mahmood, and K. Zhang, "2D MXene-Based Biosensing: a Review," *Small* 19, no. 2 (2023): 2205249, https://doi.org/10.1002/smll.202205249.

90. Z. U. D. Babar, B. Ventura Della, R. Velotta, and V. Iannotti, "Advances and Emerging Challenges in MXenes and Their Nanocom-

16163028, 2026, 46, Downloaded from https://advanced.onlinelibrary.wiley.com/doi/10.1002/adfm.75402 by University Degli Studi Di Genova, Wiley Online Library on [28/06/2026]. See the Terms and Conditions (https://onlinelibrary.wiley.com/terms-and-conditions) on Wiley Online Library for rules of use; OA articles are governed by the applicable Creative Commons License

posites for Biosensing Applications," *RSC advances* 12, no. 30 (2022): 19590–19610.

91. A. Chen and B. Shah, "Electrochemical Sensing and Biosensing Based on Square Wave Voltammetry," *Analytical Methods* 5, no. 9 (2013): 2158–2173, https://doi.org/10.1039/c3ay40155c.

92. U. Siwakoti, M. Y. Pwint, A. M. Broussard, D. R. Rivera, X. T. Cui, and E. Castagnola, "Batch-fabricated Full Glassy Carbon Fibers for Real-time Tonic and Phasic Dopamine Detection," *Frontiers in Bioengineering and Biotechnology* 13 (2025): 1543882, https://doi.org/10.3389/fbioe.2025.1543882.

93. I. M. Taylor, A. Jaquins-Gerstl, S. R. Sesack, and A. C. Michael, "Domain-Dependent Effects of DAT Inhibition in the Rat Dorsal Striatum," *Journal of Neurochemistry* 122, no. 2 (2012): 283–294, https://doi.org/10.1111/j.1471-4159.2012.07774.x.

94. J. A. Johnson, N. T. Rodeberg, and R. M. Wightman, "Measurement of Basal Neurotransmitter Levels Using Convolution-based Nonfaradaic Current Removal," *Analytical Chemistry* 90, no. 12 (2018): 7181–7189, https://doi.org/10.1021/acs.analchem.7b04682.

95. C. W. Atcherley, K. M. Wood, K. L. Parent, P. Hashemi, and M. L. Heien, "The Coaction of Tonic and Phasic Dopamine Dynamics," *Chemical Communications* 51, no. 12 (2015): 2235–2238, https://doi.org/10.1039/C4CC06165A.

96. A. Abdalla, C. W. Atcherley, P. Pathirathna, et al., "In Vivo Ambient Serotonin Measurements at Carbon-fiber Microelectrodes," *Analytical chemistry* 89, no. 18 (2017): 9703–9711, https://doi.org/10.1021/acs.analchem.7b01257.

97. E. Castagnola, Q. Cao, E. Robbins, et al., "Glassy Carbon Fiber-Like Multielectrode Arrays for Neurochemical Sensing and Electrophysiology Recording," *Advanced Materials Technologies* 10 (2024): 2400863.

98. P. P. Balasubramani, V. S. Chakravarthy, B. Ravindran, and A. A. Moustafa, "A Network Model of Basal Ganglia for Understanding the Roles of Dopamine and Serotonin in Reward-punishment-risk Based Decision Making," *Frontiers in Computational Neuroscience* 9 (2015): 76, https://doi.org/10.3389/fncom.2015.00076.

99. A. G. Fischer and M. Ullsperger, "An Update on the Role of Serotonin and Its Interplay with Dopamine for Reward," *Frontiers in Human Neuroscience* 11 (2017): 484, https://doi.org/10.3389/fnhum.2017.00484.

100. I. Boileau, J. J. Warsh, M. Guttman, et al., "Elevated Serotonin Transporter Binding in Depressed Patients with Parkinson's Disease: a Preliminary PET Study with [^{11}C] DASB," *Movement disorders: official journal of the Movement Disorder Society* 23, no. 12 (2008): 1776–1780.

101. V. Niederkofler, T. E. Asher, and S. M. Dymecki, "Functional Interplay between Dopaminergic and Serotonergic Neuronal Systems during Development and Adulthood," *ACS Chemical Neuroscience* 6, no. 7 (2015): 1055–1070, https://doi.org/10.1021/acschemneuro.5b00021.

102. E. Dremencov, I. Gispan-Herman, M. Rosenstein, et al., "The Serotonin–dopamine Interaction Is Critical for Fast-onset Action of Antidepressant Treatment: in Vivo Studies in an Animal Model of Depression," *Progress in Neuro-Psychopharmacology and Biological Psychiatry* 28, no. 1 (2004): 141–147, https://doi.org/10.1016/j.pnpbp.2003.09.030.

103. B. K. Swamy and B. J. Venton, "Carbon Nanotube-modified Microelectrodes for Simultaneous Detection of Dopamine and Serotonin in Vivo," *The Analyst* 132, no. 9 (2007): 876–884, https://doi.org/10.1039/b705552h.

104. F.-M. Zhou, Y. Liang, R. Salas, L. Zhang, M. De Biasi, and J. A. Dani, "Corelease of Dopamine and Serotonin from Striatal Dopamine Terminals," *Neuron* 46, no. 1 (2005): 65–74, https://doi.org/10.1016/j.neuron.2005.02.010.

105. F. Gonon, F. Navarre, and M. Buda, "In Vivo Monitoring of Dopamine Release in the Rat Brain with Differential Normal Pulse Voltammetry," *Analytical Chemistry* 56, no. 3 (1984): 573–575, https://doi.org/10.1021/ac00267a060.

106. C. W. Atcherley, N. D. Laude, K. L. Parent, and M. L. Heien, "Fast-scan Controlled-adsorption Voltammetry for the Quantification of Absolute Concentrations and Adsorption Dynamics," *Langmuir* 29, no. 48 (2013): 14885–14892, https://doi.org/10.1021/la402686s.

107. R. Fuller and S. Hemrick-Luecke, "Elevation of Epinephrine Concentration in Rat Brain by LY51641, a Selective Inhibitor of Type A Monoamine Oxidase," *Research Communications in Chemical Pathology and Pharmacology* 32, no. 2 (1981): 207–221.

108. I. Mefford, A. Oke, R. Keller, R. Adams, and G. Jonsson, "Epinephrine Distribution in human Brain," *Neuroscience Letters* 9, no. 2-3 (1978): 227–231, https://doi.org/10.1016/0304-3940(78)90077-0.

109. T. Yang, T. Shen, B. Duan, Z. Liu, and C. Wang, "In Vivo Electrochemical Biosensing Technologies for Neurochemicals: Recent Advances in Electrochemical Sensors and Devices," *ACS Sensors* 10, no. 1 (2025): 100–121, https://doi.org/10.1021/acssensors.4c03314.

110. K. Sankar, *Electrochemical Biosensors for Health and Disease Biomarkers* (Boston University, 2023).

111. P.-H. Lin and B.-R. Li, "Antifouling Strategies in Advanced Electrochemical Sensors and Biosensors," *The Analyst* 145, no. 4 (2020): 1110–1120, https://doi.org/10.1039/C9AN02017A.

112. C. Sanchez-Cano and M. Carril, "Recent Developments in the Design of Non-biofouling Coatings for Nanoparticles and Surfaces," *International Journal of Molecular Sciences* 21, no. 3 (2020): 1007, https://doi.org/10.3390/ijms21031007.

113. B. P. Jackson, S. M. Dietz, and R. M. Wightman, "Fast-scan Cyclic Voltammetry of 5-hydroxytryptamine," *Analytical Chemistry* 67, no. 6 (1995): 1115–1120, https://doi.org/10.1021/ac00102a015.

114. M. Wrona and G. Dryhurst, "Oxidation Chemistry of 5-Hydroxytryptamine Part 1 Mechanism and Products Formed at Micromolar Concentrations," *The Journal of Organic Chemistry* 52, no. 13 (1987): 2817–2825.

115. K. E. Dunham and B. J. Venton, "Improving Serotonin Fast-scan Cyclic Voltammetry Detection: New Waveforms to Reduce Electrode Fouling," *The Analyst* 145, no. 22 (2020): 7437–7446, https://doi.org/10.1039/D0AN01406K.

116. M. L. Perillo, B. Gupta, J. R. Siegenthaler, et al., "Evaluation of in Vitro Serotonin-Induced Electrochemical Fouling Performance of Boron Doped Diamond Microelectrode Using Fast-Scan Cyclic Voltammetry," *Biosensors* 14, no. 7 (2024): 352, https://doi.org/10.3390/bios14070352.

117. H. Shin, A. Goyal, J. H. Barnett, et al., "Tonic Serotonin Measurements in Vivo Using N-shaped Multiple Cyclic Square Wave Voltammetry," *Analytical chemistry* 93, no. 51 (2021): 16987–16994, https://doi.org/10.1021/acs.analchem.1c02131.

118. E. Castagnola, R. Garg, S. K. Rastogi, T. Cohen-Karni, and X. T. Cui, "3D Fuzzy Graphene Microelectrode Array for Dopamine Sensing at Sub-Cellular Spatial Resolution," *Biosensors and Bioelectronics* 191 (2021): 113440, https://doi.org/10.1016/j.bios.2021.113440.

119. S. Nuh, A. Numnuam, P. Thavarungkul, and T. Phairatana, "A Novel Microfluidic-Based OMC-PEDOT-PSS Composite Electrochemical Sensor for Continuous Dopamine Monitoring," *Biosensors* 13, no. 1 (2022): 68, https://doi.org/10.3390/bios13010068.

120. A. L. Hensley, A. R. Colley, and A. E. Ross, "Real-time Detection of Melatonin Using Fast-scan Cyclic Voltammetry," *Analytical Chemistry* 90, no. 14 (2018): 8642–8650, https://doi.org/10.1021/acs.analchem.8b01976.

121. P. Kokoskarova, L. Stojanov, K. Najkov, et al., "Square-wave Voltammetry of Human Blood Serum," *Scientific Reports* 13, no. 1 (2023): 8485, https://doi.org/10.1038/s41598-023-34350-1.

122. M. Naguib, V. N. Mochalin, M. W. Barsoum, and Y. Gogotsi, "25th Anniversary Article: MXenes: a New Family of Two-Dimensional Materials," *Advanced Materials* 26, no. 7 (2014): 992–1005, https://doi.org/10.1002/adma.201304138.

16163028, 2026, 46, Downloaded from https://advanced.onlinelibrary.wiley.com/doi/10.1002/adfm.75402 by University Degli Studi Di Genova, Wiley Online Library on [28/06/2026]. See the Terms and Conditions (https://onlinelibrary.wiley.com/terms-and-conditions) on Wiley Online Library for rules of use; OA articles are governed by the applicable Creative Commons License

123. B. Anasori, M. R. Lukatskaya, and Y. Gogotsi, "2D Metal Carbides and Nitrides (MXenes) for Energy Storage," in *MXenes* (Jenny Stanford Publishing, 2023), 677–722, https://doi.org/10.1201/9781003306511.

124. R. S. Azam, D. A. Almasri, R. Alfahel, et al., "MXene (Ti3C2Tx)/Cellulose Acetate Mixed-Matrix Membrane Enhances Fouling Resistance and Rejection in the Crossflow Filtration Process," *Membranes* 12, no. 4 (2022): 406, https://doi.org/10.3390/membranes12040406.

125. L. Zhang, C. Li, Y. Yang, et al., "Anti-biofouling Ti3C2TX MXene-holey Graphene Modified Electrode for Dopamine Sensing in Complex Biological Fluids," *Talanta* 247 (2022): 123614, https://doi.org/10.1016/j.talanta.2022.123614.

126. E. Castagnola, K. Woeppel, A. Golabchi, et al., "Electrochemical Detection of Exogenously Administered Melatonin in the Brain," *The Analyst* 145, no. 7 (2020): 2612–2620, https://doi.org/10.1039/D0AN00051E.

127. S. Ansah, R. S. Raman, T. Akhmetshina, and J. F. Löffler, "Effects of Bovine Serum Albumin Addition to Hanks′ solution in the Degradation of Lean Mg–Ca Alloys Used for Biodegradable Implants," *Journal of Materials Science & Technology* 251 (2025): 89–97.

128. P. Cheng, N. Ferrell, C. M. Öberg, et al., "High-Performance Hemofiltration via Molecular Sieving and Ultra-Low Friction in Carbon Nanotube Capillary Membranes," *Advanced Functional Materials* 33, no. 50 (2023): 2304672, https://doi.org/10.1002/adfm.202304672.

129. K. Jayanthi, P. Pazhanisami, K. Parthipan, et al., "Synthesis, Characterization, BSA Adsorption and Antifouling Studies of N-cyclohexylacrylamide Based Hydrogels," *Hybrid Advances* 11 (2025): 100574.

130. J. Van De Wouw and J. A. Joles, "Albumin Is an Interface between Blood Plasma and Cell Membrane, and Not Just a Sponge," *Clinical Kidney Journal* 15, no. 4 (2022): 624–634, https://doi.org/10.1093/ckj/sfab194.

131. Y. Zhang, Y. Fung, H. Sun, D. Zhu, and S. Yao, "Study of Protein Adsorption on Polymer Coatings Surface by Combining Quartz Crystal Microbalance with Electrochemical Impedance Methods," *Sensors and Actuators B: Chemical* 108, no. 1-2 (2005): 933–942, https://doi.org/10.1016/j.snb.2004.12.123.

132. D. Quezada, B. Herrera, R. Santibáñez, et al., "Impedimetric Sensor for SARS-CoV-2 Spike Protein Detection: Performance Assessment with an ACE2 Peptide-Mimic/Graphite Interface," *Biosensors* 14, no. 12 (2024): 592, https://doi.org/10.3390/bios14120592.

133. Y. Oh, M. L. Heien, C. Park, et al., "Tracking Tonic Dopamine Levels in Vivo Using Multiple Cyclic Square Wave Voltammetry," *Biosensors and Bioelectronics* 121 (2018): 174–182, https://doi.org/10.1016/j.bios.2018.08.034.

134. Y. Schmitz, M. Benoit-Marand, F. Gonon, and D. Sulzer, "Presynaptic Regulation of Dopaminergic Neurotransmission," *Journal of neurochemistry* 87, no. 2 (2003): 273–289, https://doi.org/10.1046/j.1471-4159.2003.02050.x.

135. R. W. Invernizzi, C. Garavaglia, and R. Samanin, "The α2-adrenoceptor Antagonist Idazoxan Reverses Catalepsy Induced by Haloperidol in Rats Independent of Striatal Dopamine Release: Role of Serotonergic Mechanisms," *Neuropsychopharmacology* 28, no. 5 (2003): 872–879, https://doi.org/10.1038/sj.npp.1300119.

136. S. H. Walters, E. M. Robbins, and A. C. Michael, "Kinetic Diversity of Striatal Dopamine: Evidence from a Novel Protocol for Voltammetry," *ACS Chemical Neuroscience* 7, no. 5 (2016): 662–667, https://doi.org/10.1021/acschemneuro.6b00020.

137. T. A. Mathews, D. E. Fedele, F. M. Coppelli, A. M. Avila, D. L. Murphy, and A. M. Andrews, "Gene Dose-dependent Alterations in Extraneuronal Serotonin but Not Dopamine in Mice with Reduced Serotonin Transporter Expression," *Journal of Neuroscience Methods* 140, no. 1-2 (2004): 169–181, https://doi.org/10.1016/j.jneumeth.2004.05.017.

138. K. FUXE, L. L. BUTCHER, and J. ENGEL, "DL-5-hydroxytryptophan-induced Changes in central Monoamine Neurons after Peripheral Decarboxylase Inhibition," *Journal of Pharmacy and Pharmacology* 23, no. 6 (1971): 420–424, https://doi.org/10.1111/j.2042-7158.1971.tb08673.x.

139. J. A. Stamford, Z. L. Kruk, and J. Millar, "Striatal Dopamine Terminals Release Serotonin after 5-HTP Pretreatment: in Vivo Voltammetric Data," *Brain research* 515, no. 1-2 (1990): 173–180, https://doi.org/10.1016/0006-8993(90)90593-Z.

140. H. Filik, A. A. Avan, and S. Aydar, "Square-wave Adsorptive Stripping Voltammetric Determination of Serotonin at Glassy Carbon Electrode Modified with Safranine O," *International Journal of Electrochemical Science* 9, no. 6 (2014): 2922–2933, https://doi.org/10.1016/S1452-3981(23)07979-8.

141. P. Takmakov, M. K. Zachek, R. B. Keithley, E. S. Bucher, G. S. McCarty, and R. M. Wightman, "Characterization of Local pH Changes in Brain Using Fast-scan Cyclic Voltammetry with Carbon Microelectrodes," *Analytical chemistry* 82, no. 23 (2010): 9892–9900, https://doi.org/10.1021/ac102399n.

142. K. Alex and E. Pehek, "Pharmacologic Mechanisms of Serotonergic Regulation of Dopamine Neurotransmission," *Pharmacology & Therapeutics* 113, no. 2 (2007): 296–320, https://doi.org/10.1016/j.pharmthera.2006.08.004.

143. G. Di Giovanni, V. Di Matteo, M. Pierucci, and E. Esposito, "Serotonin–dopamine Interaction: Electrophysiological Evidence," *Progress in Brain Research* 172 (2008): 45–71.

144. V. Di Matteo, G. Di Giovanni, M. Pierucci, and E. Esposito, "Serotonin Control of central Dopaminergic Function: Focus on in Vivo Microdialysis Studies," *Progress in Brain Research* 172 (2008): 7–44.

145. G. Hong and C. M. Lieber, "Novel Electrode Technologies for Neural Recordings," *Nature Reviews Neuroscience* 20, no. 6 (2019): 330–345, https://doi.org/10.1038/s41583-019-0140-6.

146. V. Viswam, M. E. J. Obien, F. Franke, U. Frey, and A. Hierlemann, "Optimal Electrode Size for Multi-scale Extracellular-potential Recording from Neuronal Assemblies," *Frontiers in Neuroscience* 13 (2019): 385, https://doi.org/10.3389/fnins.2019.00385.

147. Q. Yang, B. Wu, E. Castagnola, et al., "Integrated Microprism and Microelectrode Array for Simultaneous Electrophysiology and Two-Photon Imaging across all Cortical Layers," *Advanced Healthcare Materials* 13 (2024): 2302362, https://doi.org/10.1002/adhm.202302362.

148. B. Wu, E. Castagnola, and X. T. Cui, "Zwitterionic Polymer Coated and Aptamer Functionalized Flexible Micro-electrode Arrays for in Vivo Cocaine Sensing and Electrophysiology," *Micromachines* 14, no. 2 (2023): 323, https://doi.org/10.3390/mi14020323.

149. X. Cui, J. F. Hetke, J. A. Wiler, D. J. Anderson, and D. C. Martin, "Electrochemical Deposition and Characterization of Conducting Polymer Polypyrrole/PSS on Multichannel Neural Probes," *Sensors and Actuators A: Physical* 93, no. 1 (2001): 8–18, https://doi.org/10.1016/S0924-4247(01)00637-9.

150. X. Cui and D. C. Martin, "Electrochemical Deposition and Characterization of Poly (3, 4-ethylenedioxythiophene) on Neural Microelectrode Arrays," *Sensors and Actuators B: Chemical* 89, no. 1-2 (2003): 92–102, https://doi.org/10.1016/S0925-4005(02)00448-3.

151. E. W. Keefer, B. R. Botterman, M. I. Romero, A. F. Rossi, and G. W. Gross, "Carbon Nanotube Coating Improves Neuronal Recordings," *Nature Nanotechnology* 3, no. 7 (2008): 434–439, https://doi.org/10.1038/nnano.2008.174.

152. G. Baranauskas, E. Maggiolini, E. Castagnola, et al., "Carbon Nanotube Composite Coating of Neural Microelectrodes Preferentially Improves the Multiunit Signal-to-noise Ratio," *Journal of Neural Engineering* 8, no. 6 (2011): 066013, https://doi.org/10.1088/1741-2560/8/6/066013.

16163028, 2026, 46, Downloaded from https://advanced.onlinelibrary.wiley.com/doi/10.1002/adfm.75402 by University Degli Studi Di Genova, Wiley Online Library on [28/06/2026]. See the Terms and Conditions (https://onlinelibrary.wiley.com/terms-and-conditions) on Wiley Online Library for rules of use; OA articles are governed by the applicable Creative Commons License

153. E. Castagnola, A. Ansaldo, E. Maggiolini, et al., "Smaller, Softer, Lower-Impedance Electrodes for Human Neuroprosthesis: a Pragmatic Approach," *Frontiers in Neuroengineering* 7 (2014): 8, https://doi.org/10.3389/fneng.2014.00008.

Supporting Information

Additional supporting information can be found online in the Supporting Information section.

Supporting File: adfm75402-sup-0001-SuppMat.docx.

16163028, 2026, 46, Downloaded from https://advanced.onlinelibrary.wiley.com/doi/10.1002/adfm.75402 by University Degli Studi Di Genova, Wiley Online Library on [28/06/2026]. See the Terms and Conditions (https://onlinelibrary.wiley.com/terms-and-conditions) on Wiley Online Library for rules of use; OA articles are governed by the applicable Creative Commons License